nature structural & molecular biology

Article

https://doi.org/10.1038/s41594-025-01540-6

Mesoscale regulation of microtubule-organizing centers by the E3 ligase TRIM37

Received: 5 September 2024

Accepted: 19 March 2025

Published online: 25 May 2025

Check for updates

Zhong Y. Yeow[1] ✉, Sonia Sarju[1], Fang-Chi Chang[1], Lance Y. Xu[1], Mark van Breugel[2] & Andrew J. Holland[1] ✉

Centrosomes ensure accurate chromosome segregation during cell division. Although the regulation of centrosome number is well established, less is known about the suppression of noncentrosomal microtubule-organizing centers (ncMTOCs). The E3 ligase TRIM37, implicated in Mulibrey nanism and 17q23-amplified cancers, has emerged as a key regulator of both centrosomes and ncMTOCs. Yet, the mechanism by which TRIM37 achieves enzymatic activation to target these mesoscale structures had thus far remained unknown. Here we elucidate the activation process of TRIM37, unveiling a process that initiates with TRAF domain-directed substrate recognition followed by B-box domain-mediated oligomerization and culminates in RING domain dimerization. Using optogenetics, we demonstrate that the E3 activity of TRIM37 is directly coupled to the assembly state of its substrates, being activated only when centrosomal proteins cluster into higher-order assemblies resembling MTOCs. This regulatory framework provides a mechanistic basis for understanding TRIM37-driven pathologies and echoes the restriction of the human immunodeficiency virus capsid by TRIM5, thus unveiling a conserved activation blueprint among TRIM proteins to control turnover of complexes assembled at the mesoscale level.

Mesoscale protein assemblies serve as organizational hubs that dictate the spatial arrangement of subcellular components. The centrosome is one prominent example, serving as the primary microtubule-organizing center (MTOC) in animal cells that orchestrates the accurate segregation of chromosomes during cell division[1]. Centrosomes consist of a pair of centrioles nestled within a proteinaceous matrix known as the pericentriolar material (PCM). The PCM is an assembly of several hundred proteins that collectively act to anchor and nucleate microtubules[2,3]. Recent advancements in super-resolution microscopy have shown that the interphase PCM comprises an organized assembly of radial protein layers surrounding the centriole[4].

Centrosome number is rigorously controlled in tandem with dynamic changes in the PCM's composition and volume as cells progress through the cell cycle[5,6]. This intricate regulation underpins the centrosome's crucial function in cell division, where numerical aberrations can give rise to a range of pathologies, including cancer and neurodevelopmental disorders[7,8]. Some differentiated cell types use noncentrosomal MTOCs (ncMTOCs) in interphase for specialized functions[9]. Crucially, the presence of ncMTOCs during mitosis can threaten genome integrity[10,11] but the regulatory mechanisms governing their formation remain poorly understood[9].

TRIM37 is a member of the tripartite motif family of proteins characterized by the conserved RBCC motif, which includes a RING

[1]Department of Molecular Biology and Genetics, Johns Hopkins University School of Medicine, Baltimore, MD, USA. [2]School of Biological and Behavioural Sciences, Queen Mary University of London, London, UK. ✉e-mail: zyeow1@jhmi.edu; aholland@jhmi.edu

E3 ubiquitin ligase domain, a B-box domain and a coiled-coil domain[12]. Loss-of-function mutations in *TRIM37* cause Mulibrey nanism (MUL), a rare autosomal recessive disorder characterized by growth failure and multiorgan abnormalities[13]. Initial reports of TRIM37's localization to peroxisomes led to the classification of MUL as a peroxisomal disorder[14]. However, TRIM37-deficient mice do not display peroxisome abnormalities despite recapitulating key features of the human disease[15]. Recent work recast TRIM37 as a central player in centrosome regulation[16–18]. In the fibroblasts of persons with MUL, loss of TRIM37 causes the centriolar protein Centrobin to accumulate as a single highly structured cytoplasmic assembly. These assemblies emerge and detach from the centrosome to act as ncMTOCs that promote chromosome segregation defects—a process now implicated as a key driver of MUL pathogenesis[19,20].

While *TRIM37* loss-of-function mutations cause MUL, TRIM37 overexpression frequently occurs during tumorigenesis[21]. *TRIM37* is located within 17q23, a chromosome region often amplified in breast cancer or gained in neuroblastomas[22,23]. Amplicon-directed overexpression of TRIM37 promotes the degradation of the PCM scaffolding protein CEP192, leading to reduced PCM levels at the centrosome and an increased frequency of mitotic errors[24]. Moreover, cancer cells exhibiting elevated TRIM37 expression are therapeutically vulnerable to centrosome loss induced by Polo-like kinase 4 (PLK4) inhibition. This arises as high levels of TRIM37 impede the formation of CEP192-containing foci, an ncMTOC crucial for mitotic spindle assembly in cells lacking centrosomes[24,25]. The discovery of this synthetic lethal interaction has spurred the development of PLK4 inhibitors, now entering clinical trials to target tumors overexpressing TRIM37.

TRIM37 has emerged as a critical regulator of centrosome function that counteracts the formation of ectopic Centrobin assemblies and degrades the PCM scaffolding protein CEP192 but how TRIM37 recognizes its substrates in the form of mesoscale cellular assemblies remains unclear. Here, we demonstrate that substrate assembly promotes TRIM37 oligomerization, a pivotal step that activates its ubiquitin ligase function. This activation mechanism enables the selective degradation of centrosome proteins incorporated into higher-order assemblies, providing an elegant solution through which TRIM37 exerts control over cellular structures integral to cell division.

Results

MUL *TRIM37* mutations reveal shared MTOC regulation

TRIM37 possesses a core RBCC motif followed by a unique TRAF domain and an unstructured C-terminal tail (Fig. 1b, middle)[26]. To examine the contributions of these domains to TRIM37 function, we knocked out *TRIM37* in nontransformed RPE-1 cells and re-expressed wild-type (WT) or mutant variants of HA-tagged TRIM37. Knockout (KO) of *TRIM37* was confirmed by Sanger sequencing and loss of TRIM37 protein expression (Extended Data Fig. 1a,b). Consistent with prior reports[19,20], *TRIM37*$^{-/-}$ cells formed cytoplasmic Centrobin assemblies (Fig. 1a and Extended Data Fig. 1c, left) that were lost upon the expression of WT TRIM37 (Fig. 1c and Extended Data Fig. 1c). Inactivation of TRIM37 E3 ligase activity with the C18R RING domain mutation[19,24,25] prevented degradation of the Centrobin assembly without impacting the recruitment of TRIM37 to the assembly (Fig. 1c and Extended Data Fig. 1c). Clinically relevant MUL mutations within the B-box (encoding C109S)[27] and TRAF domain (encoding G322V)[28] were also defective in degrading the Centrobin assembly, supporting a causative role of this assembly in MUL pathogenesis (Fig. 1c). Notably, while the C109S B-box mutant localized to the Centrobin assembly, the G322V TRAF mutant did not (Extended Data Fig. 1c).

To assess the relevance of these findings in the context of 17q23-amplified cancers, we monitored the impact of doxycycline-induced overexpression of TRIM37 on the abundance of its centrosomal substrate CEP192 (Fig. 1a). Expression of WT TRIM37 in RPE-1 cells drove a significant reduction in CEP192 levels at the centrosome (Fig. 1b,d). In contrast, TRIM37 C18R, C109S and G322V mutants were ineffective at degrading centrosomal CEP192 (Fig. 1b,d). Reflecting the localization patterns seen with the Centrobin assembly, both the TRIM37 C18R RING and the C109S B-box mutants localized to the centrosome, while the G322V TRAF mutant failed to do so (Fig. 1b). Deletion of the B-box or TRAF domain (ΔB-box and ΔTRAF) phenocopied the effects of the respective MUL point mutants (Fig. 1b,d and Extended Data Fig. 1d,e), indicating that these mutations lead to domain-specific loss of function in TRIM37. Collectively, these data suggest that TRIM37 uses a common mechanism for the recognition and subsequent degradation of Centrobin in cytoplasmic assemblies and CEP192 incorporated into centrosomes.

TRIM37 TRAF domain directs centrosomal substrate recognition

The TRIM family member TRIM5 is known for its role in inhibiting retroviral infections, particularly human immunodeficiency virus (HIV)[29]. TRIM5 and TRIM37 have a similar domain organization, except that the TRAF domain of TRIM37 is replaced by a SPRY domain in TRIM5. TRIM5 assembles into a dimer, with the two SPRY domains centrally located and each monomer's RING and B-box domains positioned at opposite ends of an antiparallel coiled coil[30,31]. As RING dimerization is crucial for E3 ligase activity, this antiparallel configuration prevents the interaction of the two RING domains within a single TRIM5 dimer. E3 activation occurs when many TRIM5 dimers bind to the surface of the viral capsid through the SPRY domain and assemble into an oligomeric lattice. This facilitates the dimerization of RING domains from adjacent TRIM5 dimers and subsequent E3 ligase activity[32,33]. The crystal structure of the TRIM37 RING dimer closely resembles that of TRIM5 (ref. 33). Moreover, AlphaFold2 modeling[34] predicted an antiparallel TRIM37 dimer that was similar to TRIM5, with the TRIM37 TRAF domain occupying the position of the TRIM5 SPRY domain (Fig. 1e).

Given that mutation or deletion of the TRIM37 TRAF domain prevented recruitment of TRIM37 to Centrobin assemblies and the centrosome, the TRAF domain is likely to be the substrate recognition motif of TRIM37.

To identify TRAF domain-mediated proximity interactors of TRIM37, we performed biotin labeling with mTurbo-tagged TRIM37 (Fig. 2a,b). We hypothesized that the C18R RING mutant would show extensive labeling of centrosome substrates because of its impaired ability to promote substrate degradation, while the G322V TRAF mutant would exhibit a reduced labeling profile. After background subtraction, we curated a list of 98 high-confidence proteins that are in close spatial proximity to TRIM37 when it is targeted to the centrosome by the TRAF domain (Fig. 2c,d). Of these interactors, 74% (73/98) overlapped with published centrosome proximity datasets[35,36], with CEP192 and Centrobin among the most enriched proteins (Fig. 2d). Gene Ontology (GO) analysis further emphasized the significant enrichment of centrosome and ciliary proteins within the TRIM37 proximity interactome (Fig. 2e), underscoring the central role of the TRIM37 TRAF domain in centrosomal substrate targeting.

SPRY–TRAF swap repurposes antiviral TRIM5 for MTOC control

If TRIM5 and TRIM37 share structural and regulatory principles, we reasoned that we could impart the regulation of TRIM37 substrates by swapping the TRIM5 SPRY domain with the TRIM37 TRAF domain (Fig. 3a). TRIM5 did not localize to the centrosome and could not degrade CEP192 (Fig. 3b–d). By contrast, the TRIM5–TRAF chimera localized to the centrosome and degraded CEP192 to a similar extent to TRIM37 (Fig. 3b–d). Moreover, introducing the MUL TRAF domain mutation (G322V) into the TRIM5–TRAF chimera abolished its centrosomal localization and capacity to degrade CEP192 (Fig. 3b–d). Similar findings were observed with the degradation of the Centrobin assembly in *TRIM37*$^{-/-}$ cells (Fig. 3e,f). These data support the proposal that TRIM37 functions analogously to TRIM5, with the TRAF domain being key for the selective regulation of MTOCs.

https://doi.org/10.1038/s41594-025-01540-6

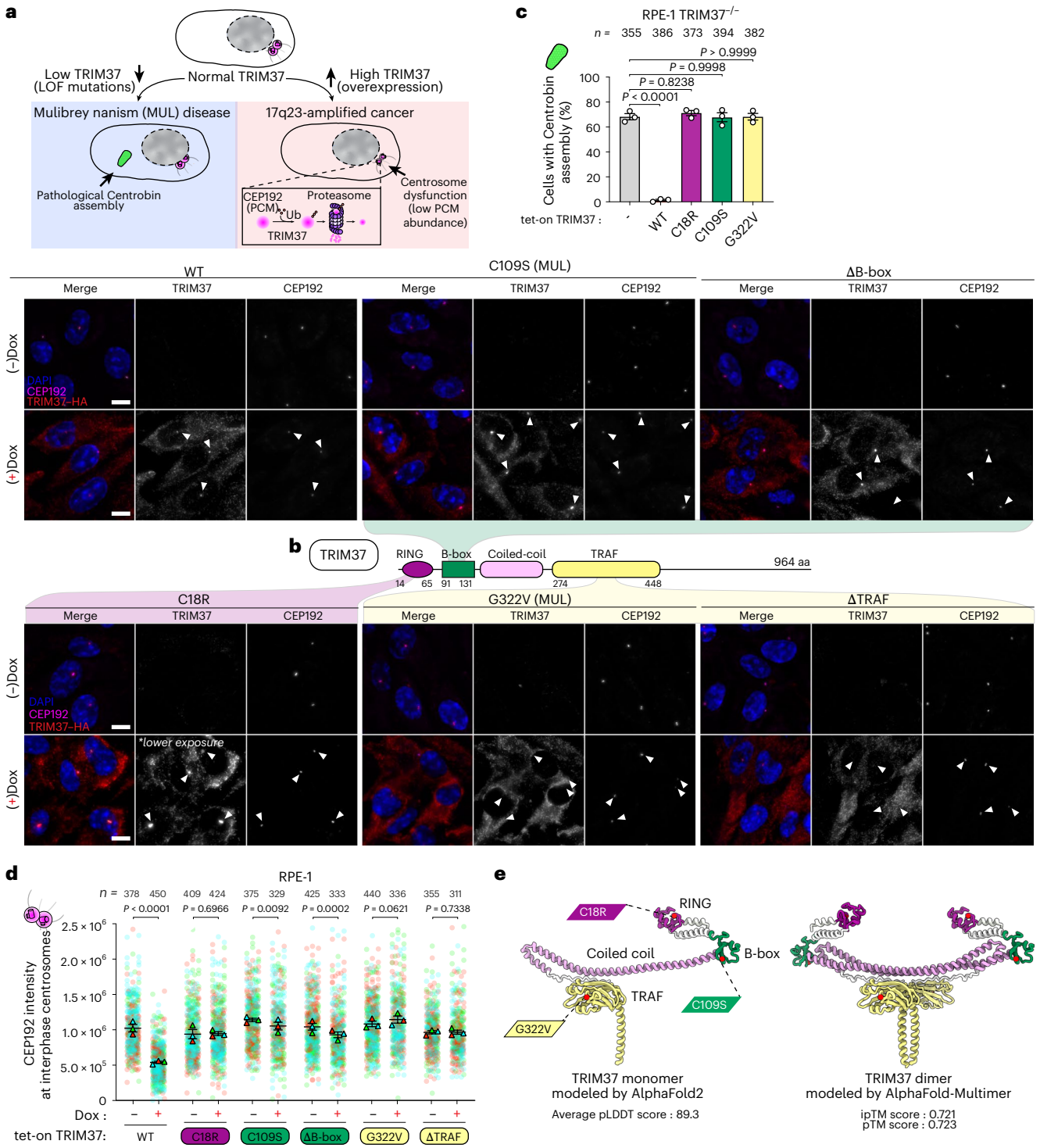

Fig. 1 | Domain-specific impact of MUL *TRIM37* mutations on MTOC regulation. **a**, Diagram depicting TRIM37 dysregulation in MUL and 17q23-amplified cancers. In MUL, *TRIM37* loss-of-function mutations result in the aberrant formation of Centrobin assemblies, which act as ectopic MTOCs during mitosis. Conversely, in 17q23-amplified cancers, elevated expression of TRIM37 leads to excessive degradation of centrosomal CEP192. **b**, Middle: domain architecture of TRIM37 (UniProt O94972) highlighting the common RBCC motif and unique C-terminal TRAF domain. Top and bottom: localization pattern and effect of HA-tagged TRIM37 variants (domain-specific mutations and deletions) on centrosomal CEP192 levels in RPE-1 tet-on TRIM37 cells. Arrows indicate the positions of centrosomes. Data are representative of $n = 3$ biological replicates. Scale bars, 5 µm. **c**, Quantification of Centrobin assembly occurrence in RPE-1 *TRIM37*$^{-/-}$ cells expressing the indicated HA-tagged TRIM37 variants ($n = 3$ biological replicates, each with >100 cells). *P* values were determined using a one-way analysis of variance (ANOVA) with a post hoc Dunnett's multiple-comparisons test to evaluate differences between the TRIM37 variants and WT. Data represent the mean ± s.e.m. **d**, Quantification of centrosomal CEP192 signal in RPE-1 tet-on TRIM37 cells from **b** ($n = 3$ biological replicates, each with >80 cells). *P* values were determined using an unpaired two-tailed *t*-test. Data represent the mean ± s.e.m. **e**, Left: AlphaFold-predicted monomer of TRIM37. The RING, B-box, coiled-coil and TRAF domains are shown, with mutated residues highlighted in red. Right: AlphaFold-Multimer-predicted model of a TRIM37 dimer. For both models, the unstructured C-terminal tail of TRIM37 (residues 449–964) is not shown because of the lack of a high-confidence prediction. pLDDT, predicted local distance difference test; pTM, predicted template modeling.

https://doi.org/10.1038/s41594-025-01540-6

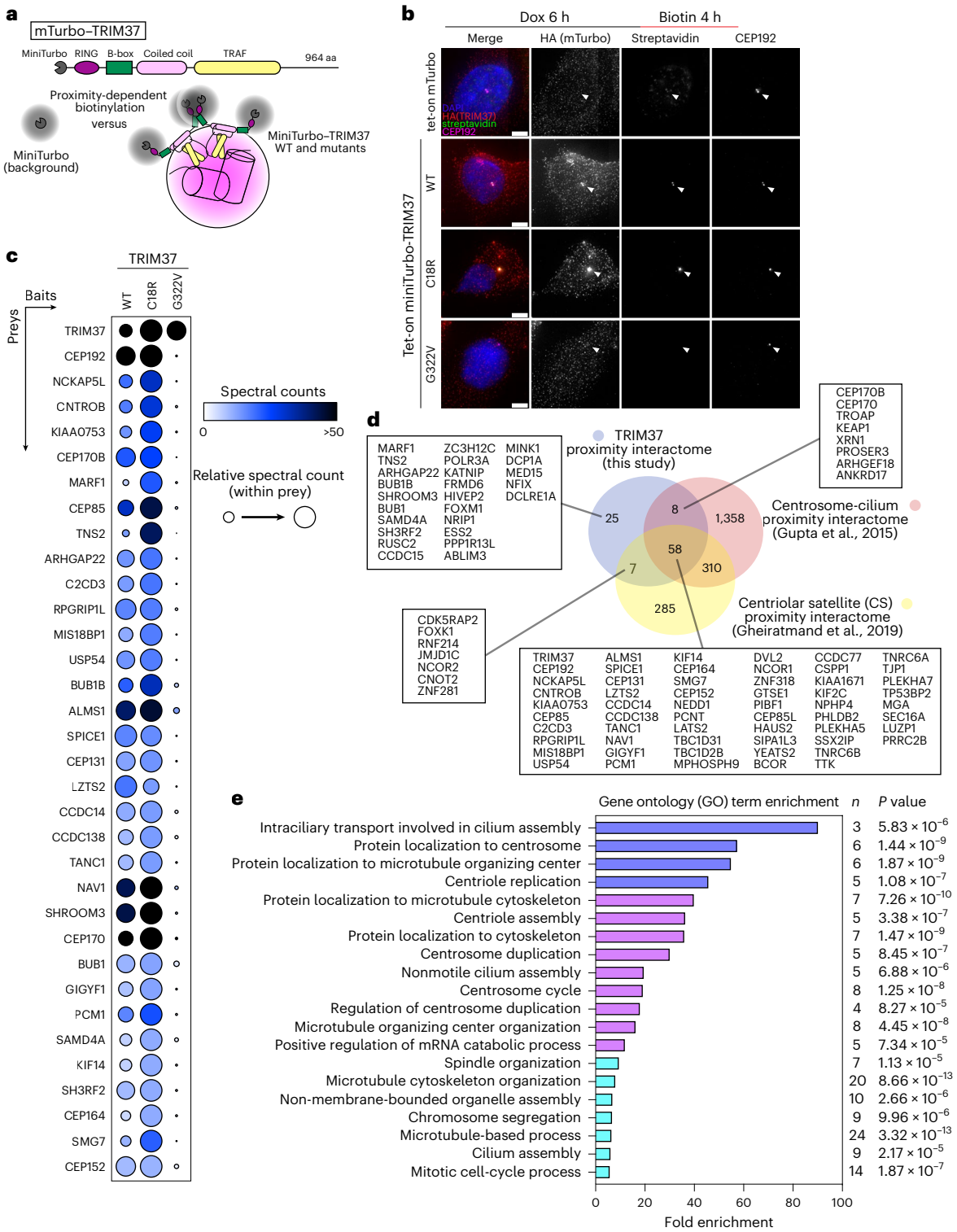

Fig. 2 | Proximity-dependent BioID identifies TRAF domain interactors of TRIM37. a, Top: schematic of miniTurbo–TRIM37 construct used for BioID labeling experiments. Bottom: depiction of the approach to isolate TRAF domain-specific interactors of TRIM37. **b**, Immunofluorescence images of biotin-labeled proteins in RPE-1 cells expressing the indicated constructs. Streptavidin staining indicates biotinylated proteins, with centrosomes marked by CEP192 staining. Arrows indicate the positions of centrosomes. Data are representative of $n = 2$ biological replicates. Scale bars, 5 µm. **c**, Thresholded MS results displaying the top 34 proximity interactors (TRAF domain specific) by spectral count. Interactors were identified using filters detailed in Methods. **d**, Venn diagram illustrating the overlap between TRIM37 TRAF domain-specific proximity interactome and two published centrosome proximity interactomes. **e**, GO analysis of data from BioID experiments. *P* values were determined using a binomial test with false discovery rate correction for multiple comparisons.

https://doi.org/10.1038/s41594-025-01540-6

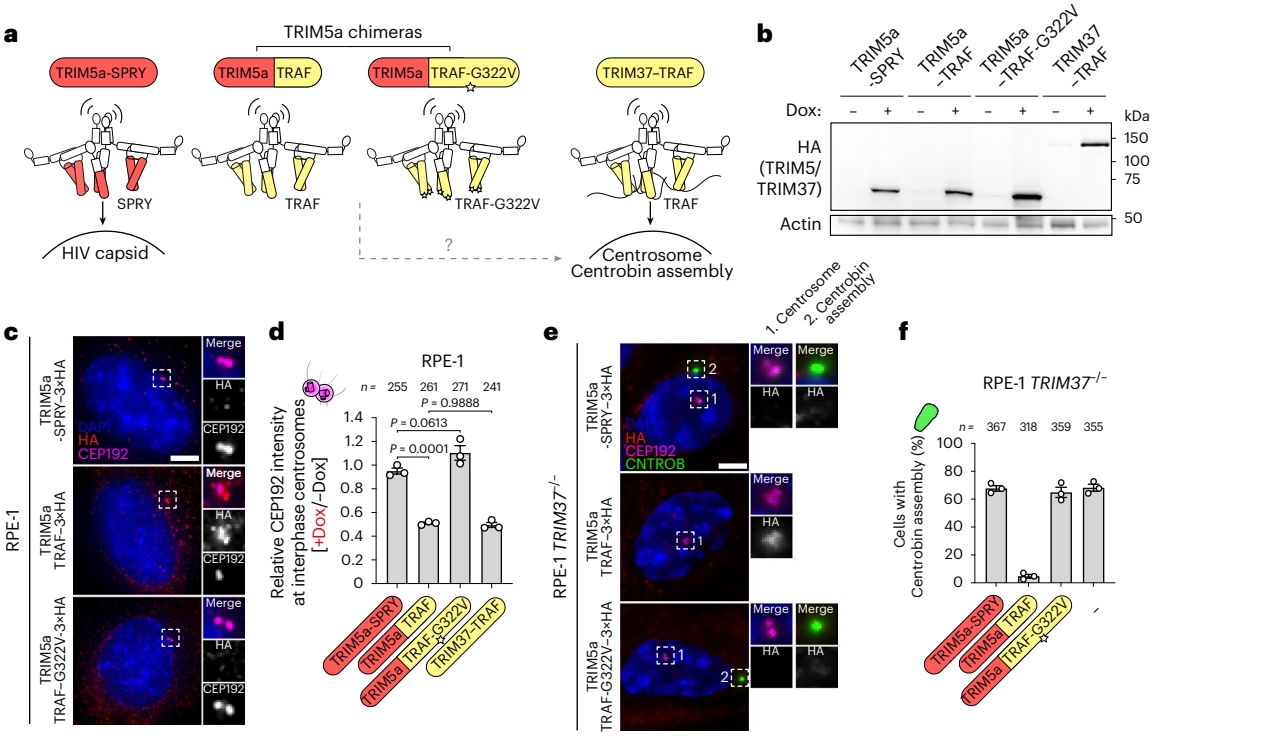

Fig. 3 | Chimeric TRIM5 bearing the TRIM37 TRAF domain regulates MTOCs. **a**, Schematic overview of the domain swap strategy, which replaces the TRIM5 SPRY domain with the TRIM37 TRAF domain to generate a chimeric TRIM5–TRAF protein. **b**, Immunoblot showing total protein expression levels of indicated HA-tagged TRIM5 constructs in RPE-1 tet-on TRIM5 cells. Actin was used as a loading control. Data are representative of $n = 3$ biological replicates. **c**, Representative images of the localization and effect of indicated HA-tagged TRIM5 constructs on centrosomal CEP192 levels in RPE-1 tet-on TRIM5 cells. Data are representative of $n = 3$ biological replicates. Scale bar, 5 µm. **d**, Quantification of centrosomal CEP192 signal upon doxycycline-induced expression of indicated constructs in RPE-1 tet-on TRIM5 cells from **c**, with TRIM37 included as a benchmark ($n = 3$ biological replicates, each with >80 cells). *P* values were determined using a one-way ANOVA with a post hoc Tukey's multiple-comparisons test. Data represent the mean ± s.e.m. **e**, Representative images of RPE-1 *TRIM37*$^{-/-}$ cells expressing the indicated HA-tagged TRIM5 constructs. Inset 1 denotes the centrosome, marked by CEP192, and inset 2 denotes the Centrobin assembly, identified by intense Centrobin staining that is not localized to the centrosome. Data are representative of $n = 3$ biological replicates. Scale bar, 5 µm. **f**, Quantification of Centrobin assembly occurrence in RPE-1 *TRIM37*$^{-/-}$ cells expressing the indicated HA-tagged TRIM5 constructs from **e** ($n = 3$ biological replicates, each with >100 cells). Data represent the mean ± s.e.m.

TRIM37 undergoes centrosome-templated oligomerization

We posited that TRIM37 forms higher-order assemblies crucial for centrosome regulation. Immunoblotting of HA–TRIM37 in RPE-1 whole-cell lysates revealed a band migrating at ~130 kDa corresponding to monomeric TRIM37 and a distinct higher-molecular-weight (HMW) species formed by the RING C18R TRIM37 mutant that migrated >250 kDa (Extended Data Fig. 2a). The TRIM37 HMW species was absent in the MUL B-box C109S or TRAF G322V mutants (Extended Data Fig. 2a). We hypothesized that catalytically dead C18R TRIM37 undergoes substrate-templated oligomerization but does not autodegrade, explaining the presence of HMW protein. Consistently, proteasomal inhibition with MG132 prevented the self-degradation of WT TRIM37 and enabled the formation of HMW species (Extended Data Fig. 2b). To investigate whether the HMW species of TRIM37 is enriched at the centrosome, we purified centrosomes from RPE-1 cells expressing the RING C18R or RING–TRAF (C18R;G322V double mutant of HA–TRIM37 (Fig. 4a,b). We observed a significant enrichment of monomeric and HMW TRIM37 C18R in the centrosomal fraction compared to the cytoplasmic and nuclear fractions (Fig. 4c,d). Conversely, TRIM37 C18R;G322V did not localize to the centrosome and remained primarily in the cytoplasmic fraction (Fig. 4b–d), suggesting that TRAF-mediated centrosome targeting is required for TRIM37 HMW formation.

We reasoned that the TRIM37 HMW species arises from the incomplete breakdown of the TRIM37 oligomer under denaturing SDS–PAGE conditions. To preserve the substrate-driven assemblies of TRIM37, we conducted in vivo crosslinking experiments using two crosslinkers with distinct linker arm lengths (disuccinimidyl glutarate (DSG), 7.7 Å; disuccinimidyl suberate (DSS), 11.4 Å) (Fig. 4e and Extended Data Fig. 2c). The addition of either crosslinking agent led to a concentration-dependent reduction in the free TRIM37 C18R monomer and corresponding enrichment of TRIM37 HMW forms, including putative dimers, trimers and beyond—collectively termed oligomers (Fig. 4f and Extended Data Fig. 2c). This effect was not observed with the ubiquitously expressed protein vinculin, ruling out nonspecific crosslinking activity (Fig. 4f and Extended Data Fig. 2c). Notably, the TRIM37 double mutant (C18R;G322V) with a defective TRAF domain did not display clear stabilization of TRIM37 HMW forms with either crosslinking agent (Fig. 4f and Extended Data Fig. 2c).

To extend our findings to endogenous TRIM37, we introduced the TRIM37 C18R RING mutation into RPE-1 cells using CRISPR–Cas9 (hereafter referred to as *TRIM37*^{C18R}) (Extended Data Fig. 2d). Fractionation assays confirmed the centrosomal accumulation of monomeric and HMW forms of endogenous TRIM37 C18R (Extended Data Fig. 2e). Moreover, crosslinking-dependent stabilization of additional endogenous HMW species was evident in *TRIM37*^{C18R} cells (Extended Data Fig. 2f). Overall, these findings provide support for the hypothesis that substrate binding induces the formation of higher-order TRIM37 assemblies at the centrosome.

Autodegradation impedes TRIM37 centrosomal detection

Detecting endogenous TRIM37 at the centrosomes has been challenging, with one study revealing no noticeable differences in TRIM37

https://doi.org/10.1038/s41594-025-01540-6

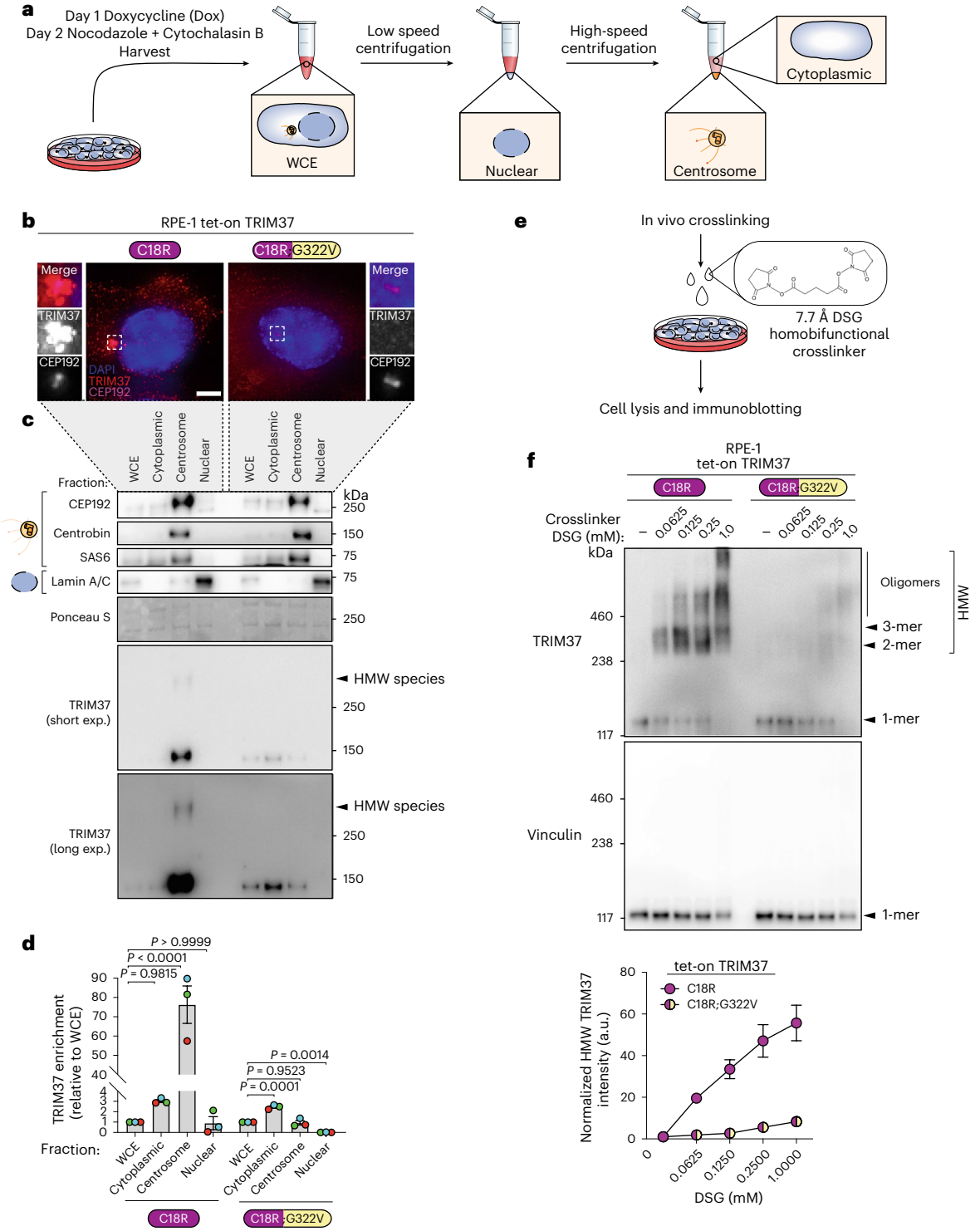

Fig. 4 | TRAF-directed higher-order assembly of TRIM37 at the centrosome. **a**, Experimental schematic of the centrosome enrichment assay used to separate nuclear, cytoplasmic and centrosomal fractions, as analyzed in **c**,**d**. **b**, Representative images of RPE-1 cells expressing the TRIM37 RING domain mutant (C18R) or TRIM37 RING–TRAF double mutant (C18R;G322V) ($n = 3$ biological replicates). Scale bar, 5 µm. **c**, Immunoblot showing TRIM37 protein levels across the indicated cellular fractions. Validation markers include CEP192, Centrobin and SAS6 for the centrosomal fraction and Lamin A/C for the nuclear fraction. The Ponceau-stained blot indicates loading. Data are representative of $n = 3$ biological replicates. WCE, whole-cell extract; exp., exposure. **d**, Densitometric analysis of immunoblot in **c** with graph depicting TRIM37 enrichment in indicated fractions relative to the WCE ($n = 3$ biological replicates). *P* values were determined using a one-way ANOVA with a post hoc Dunnett's multiple-comparisons test to evaluate the enrichment of TRIM37 in each cellular fraction relative to the WCE. Data represent the mean ± s.e.m. **e**, Schematic of the in vivo crosslinking protocol applied to RPE-1 cells using membrane-permeable crosslinkers to elucidate TRIM37 oligomerization dynamics. **f**, Top: immunoblot showing detection of various HMW species of TRIM37 upon treatment with increasing concentrations of DSG crosslinker. Vinculin was used as a loading and oligomerization control. Data are representative of $n = 2$ biological replicates. Bottom: densitometric analysis of immunoblot with a graph depicting normalized HMW TRIM37 intensity upon increasing DSG concentrations relative to DMSO control (−DSG). Data represent the mean ± s.e.m.

https://doi.org/10.1038/s41594-025-01540-6

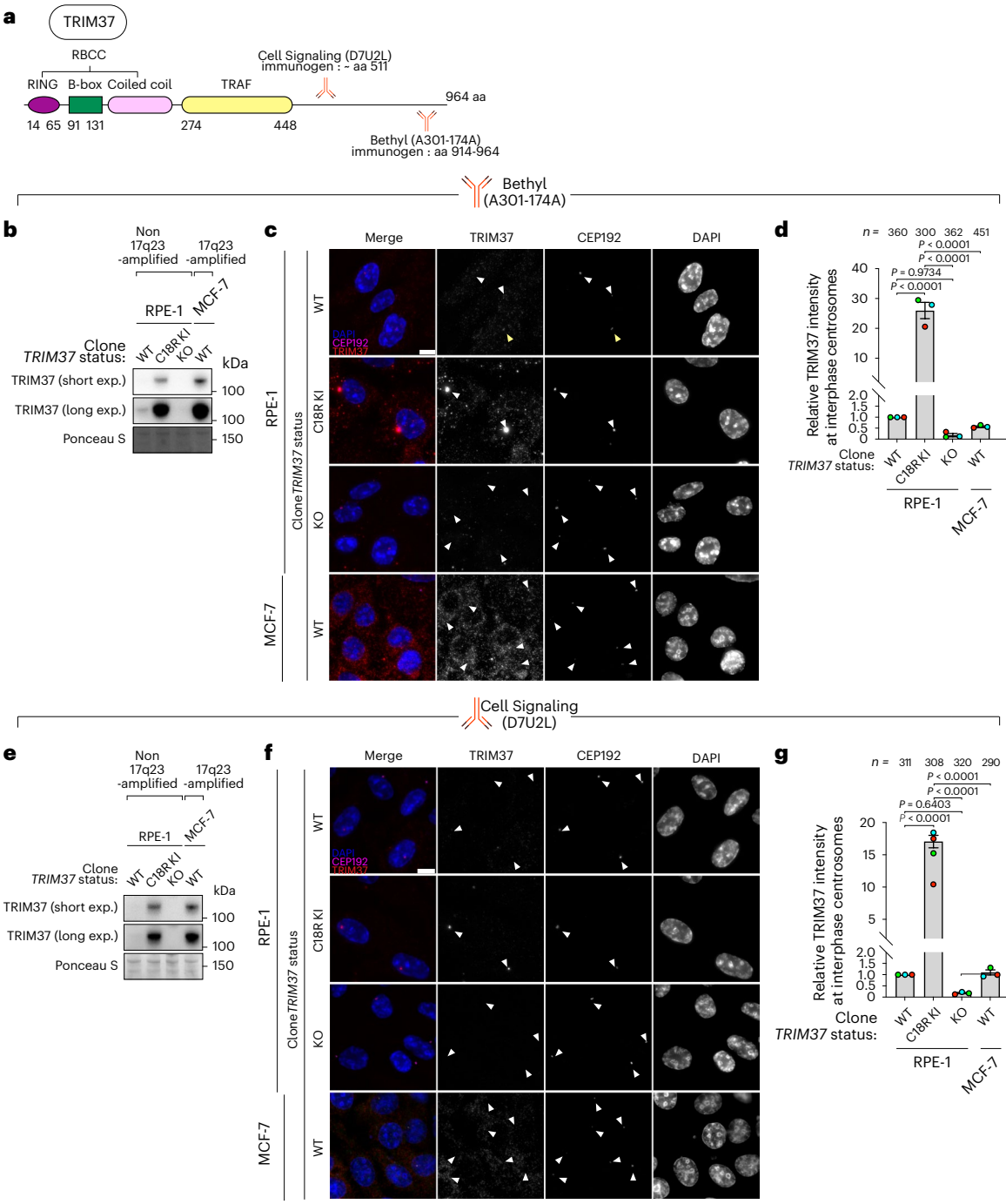

Fig. 5 | Endogenous TRIM37 localization at the centrosome is revealed by E3 ligase inactivation. a, Schematic of TRIM37, highlighting epitopes recognized by two commercial antibodies. Anti-TRIM37 antibody (Bethyl, A301-173A) was used for the experiments in **b**–**d**. **b**, Immunoblot showing endogenous TRIM37 protein levels across a panel of cell lines with the indicated *TRIM37* status. The Ponceau-stained blot indicates loading. Data are representative of $n = 3$ biological replicates. **c**, Representative images showing the immunostaining pattern of endogenous TRIM37 in the cell line panel. Arrows indicate centrosomes. Data are representative of $n = 3$ biological replicates. Scale bar, 5 µm. **d**, Quantification of endogenous TRIM37 signal at the centrosomes ($n = 3$ biological replicates, each with >100 cells). *P* values were determined using a one-way ANOVA with a post hoc Tukey's multiple-comparisons test. Data represent the mean ± s.e.m. **e**–**g**, Same as **b**–**d**, but with a second antibody (Cell Signaling Technology, D7U2L).

immunostaining between control and *TRIM37*-KO cells despite using ten different commercial antibodies[18]. Our model posits that TRIM37 undergoes oligomerization at the centrosome, triggering E3 ligase activation followed by autodegradation. Thus, we hypothesized that inactivating the RING domain would reveal stable TRIM37 enrichment at the centrosome. To test this, we assessed TRIM37 protein levels and localization across a panel of cell lines using two commercial antibodies (Fig. 5a). Consistent with prior data, we observed a diffuse and punctate pattern of endogenous WT TRIM37 in RPE-1 cells (Fig. 5b–g), with weak colocalization at the centrosome (Fig. 5c, yellow arrow). RING inactivation in RPE-1 *TRIM37*^{C18R} cells led to intense TRIM37 centrosome staining (Fig. 5b–g). This strong signal was not attributable to increased total protein levels, as 17q23-amplified MCF-7 cells overexpress TRIM37 to a higher level than the *TRIM37*^{C18R} cells yet lack

https://doi.org/10.1038/s41594-025-01540-6

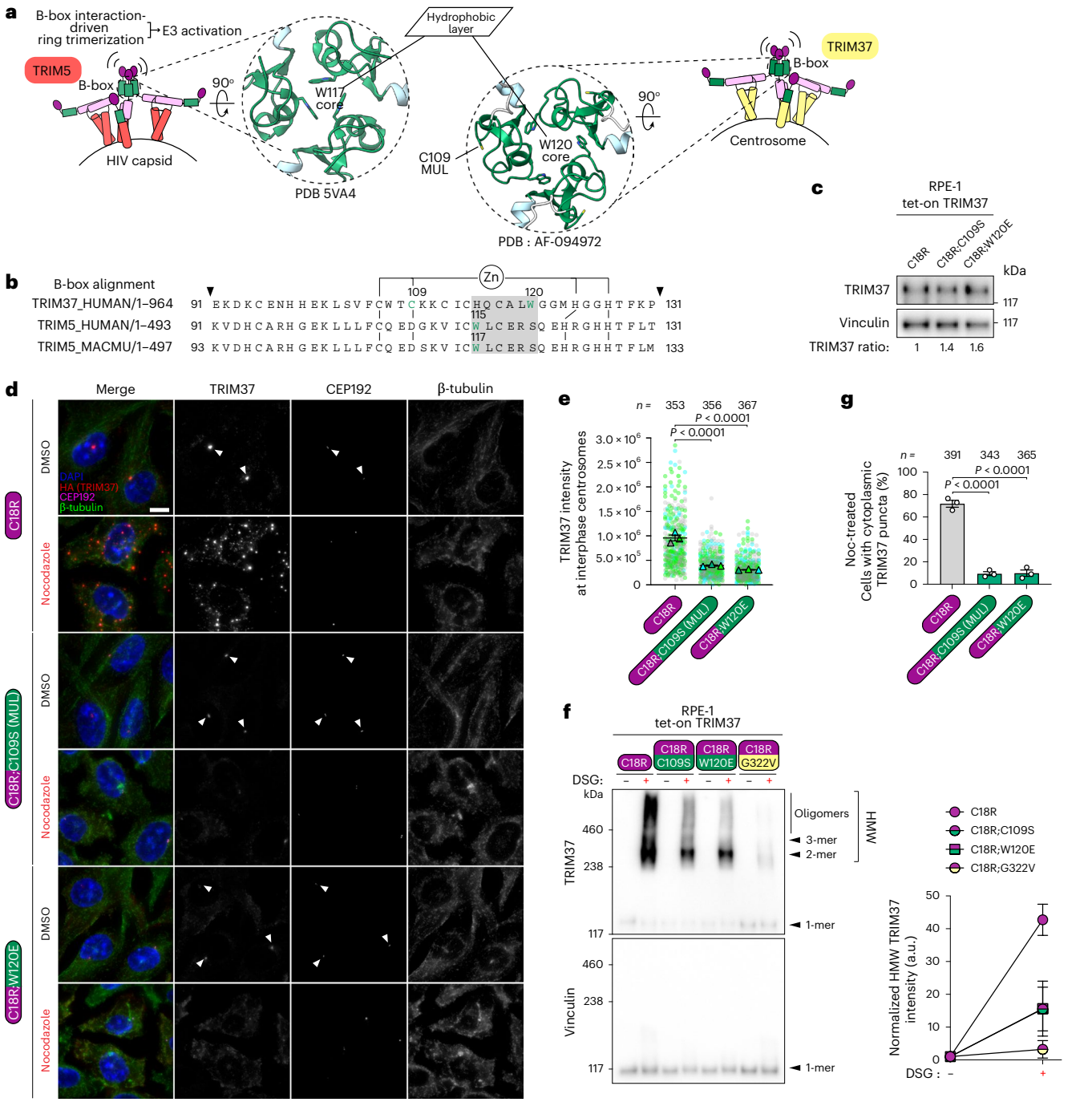

Fig. 6 | Mutations in the B-box domain impair TRIM37 higher-order assembly. **a**, Left: diagram illustrating the B-box trimerization interface of TRIM5 dimers on the HIV capsid. Trimers are stabilized by W117 residues within the hydrophobic core, as shown in the magnified top-down view of the TRIM5 B-box crystal structure (PDB 5VA4). Right: analogous diagram of a putative oligomer formed by TRIM37 dimers at the centrosome, where B-box trimerization is hypothesized to be stabilized by W120 residues, the synonymous counterpart to TRIM5's W117. A magnified top-down view shows the putative TRIM37 B-box trimer modeled by fitting AlphaFold-predicted TRIM37 monomers onto the TRIM5 crystal structure. **b**, Alignment of the B-box domains from human TRIM37 and human and rhesus macaque (*Macaca mulatta*) TRIM5. C109, mutated in MUL disease, is pivotal for Zn coordination. The gray-highlighted region denotes the sequence alignment where TRIM5 W115 and W117 residues correspond to TRIM37 W120. **c**, Immunoblot showing total protein expression levels of TRIM37 variants in RPE-1 tet-on TRIM37 cells from **d**. Vinculin was used as a loading control. Data are representative of $n = 3$ biological replicates. **d**, Representative images of RPE-1 tet-on TRIM37 cells expressing the RING domain mutant TRIM37 C18R or RING–B-box double mutants C18R;C109S and C18R;W120E. Cells were treated with DMSO (control) or nocodazole (3.3 µM) 30 min before doxycycline induction to depolymerize microtubules. Arrows indicate the positions of centrosomes ($n = 3$ biological replicates). Scale bar, 5 µm. **e**, Quantification of centrosomal TRIM37 signal in DMSO-treated cells from **d** ($n = 3$ biological replicates, each with >50 cells). *P* values were determined using a one-way ANOVA with a post hoc Dunnett's multiple-comparisons test. Data represent the mean ± s.e.m. **f**, Left: immunoblot showing detection of HMW TRIM37 species upon in vivo DSG crosslinking. Vinculin was used as a loading and oligomerization control. Data are representative of $n = 3$ biological replicates. Right: densitometric analysis of immunoblot with graph depicting normalized HMW TRIM37 intensity with DSG crosslinker (+) relative to DMSO control (−DSG). Data represent the mean ± s.e.m. **g**, Cytoplasmic TRIM37 puncta prevalence in nocodazole-treated cells from **d** ($n = 3$ biological replicates, each with >100 cells). *P* values were determined using a one-way ANOVA with a post hoc Dunnett's multiple-comparisons test. Data represent the mean ± s.e.m.

a comparable centrosomal signal (Fig. 5b–g). We conclude that the autodestruction of clustered TRIM37 likely explains the difficulty in detecting the centrosome-localized protein.

TRIM37 B-box domain mediates higher-order assembly

The B-box domain of TRIM5 is known to drive higher-order assembly through homotrimer formation, with each B-box originating from one TRIM5 dimer (Fig. 6a). These B-box–B-box interactions are mediated in part by the indole side chains of a key tryptophan residue and are pivotal for facilitating avid binding to retroviral capsids[37,38] (Fig. 6a). Structural examination of the TRIM37 B-box homotrimer (AlphaFold model) with that of TRIM5 (Protein Data Bank (PDB) 5VA4)[38], along with sequence alignment analysis, suggested that the critical tryptophan residue in the TRIM5 B-box corresponds to W120 in TRIM37 (Fig. 6a,b). This analysis also predicted that the MUL C109S amino acid mutation impacts a Zn-coordinating cysteine residue that is crucial for the proper folding of the B-box domain (Fig. 6b)[39]. Despite similar levels of expression (Fig. 6c), the C18R;W120E and C18R;C109S MUL B-box mutants of TRIM37 exhibited strongly reduced accumulation at the centrosome and impaired crosslink-stabilized HMW species compared to the RING C18R mutant alone (Fig. 6d–f). The addition of nocodazole to induce microtubule depolymerization before induction of TRIM37 expression led to the formation of multiple discrete cytoplasmic puncta of TRIM37 C18R that did not localize to the centrosome (Fig. 6d). These puncta are akin to cytoplasmic bodies formed by TRIM5 upon self-association (nontemplated assembly)[40], a process that is also B-box dependent[41,42]. Importantly, the formation of nocodazole-induced TRIM37 cytoplasmic puncta was significantly impaired in cells expressing the two TRIM37 B-box mutants (C18R;C109S and C18R;W120E) (Fig. 6d,g), underscoring the B-box's crucial role in orchestrating both templated and nontemplated higher-order assembly of TRIM37.

TRIM37 possesses a long, unstructured C-terminal tail following the TRAF domain of unknown function. To evaluate the contribution of this segment (residues 449–964) to TRIM37's activity and higher-order assembly, we engineered a truncated version of TRIM37 lacking the C terminus, hereafter referred to as miniTRIM37 (Extended Data Fig. 3a). miniTRIM37 maintained E3 ubiquitin ligase activity, as evidenced by its centrosomal localization and effective degradation of CEP192 (Extended Data Fig. 3b–d). Additionally, miniTRIM37 exhibited oligomerization properties in crosslinking experiments, showing that the core domains (RBCC and TRAF) but not the unstructured C terminus are sufficient for TRIM37's higher-order assembly (Extended Data Fig. 3e).

Sensitivity to PLK4 inhibitor requires TRIM37 oligomerization

Prior work showed that the overexpression of TRIM37 in 17q23-amplified cancers suppresses the formation of PCM foci critical for acentrosomal cell division, thereby explaining the vulnerability of these cancers to centrosome depletion by PLK4 inhibition[24]. As previously reported, treatment of MCF-7 cells with a PLK4 inhibitor resulted in greatly reduced clonogenic viability (Extended Data Fig. 4b), the appearance of shorter spindles with unfocused poles and reduced formation of noncentrosomal PCM foci (Extended Data Fig. 4c,d). These adverse effects were all rescued by TRIM37 knockdown (KD) (Extended Data Fig. 4a–d). To specifically disrupt TRIM37 higher-order assembly, we introduced the mutation encoding the C109S B-box mutant into the *TRIM37* gene in MCF-7 cells using CRISPR–Cas9. Although complete allelic conversion of the amplified *TRIM37* gene could not be achieved, sequencing revealed that approximately half of the MCF-7 *TRIM37* alleles incorporated the C109S variant (hereafter referred to as MCF-7 *TRIM37*^{C109S}) (Extended Data Fig. 4e). Importantly, *TRIM37*^{C109S} cells displayed marked resistance to PLK4 inhibition along with a corresponding improvement in the fidelity of mitotic spindle assembly in acentrosomal conditions (Extended Data Fig. 4b–d). This occurred even though *TRIM37*^{C109S} cells expressed similar levels of TRIM37 protein to WT MCF-7 cells (Extended Data Fig. 4a), implying that, while abundant, TRIM37 C109S proteins are functionally defective. These findings highlight the critical role of TRIM37's oligomerization in driving synthetic lethality with PLK4 inhibition in 17q23-amplified cancers.

Substrate-induced clustering activates TRIM37

Substrate-induced clustering is a key activation mechanism observed in several members of the TRIM protein family[43]. To directly test the role of clustering in regulating TRIM37 activity, we developed an optogenetic approach to enable spatiotemporal control of TRIM37 clustering independent of its conventional substrate interactions. We fused a TRIM37 TRAF mutant (G322V) that is impaired in substrate binding to the fluorescent reporter mNeonGreen (mNG) and CRY2clust, a variant of the cryptochrome 2 photoreceptor known for its rapid oligomerization upon blue-light exposure[44] (Extended Data Fig. 5a). Live-cell imaging demonstrated that TRIM37 G322V–mNG–CRY2 formed cytoplasmic clusters following blue-light stimulation (Extended Data Fig. 5b,c and Supplementary Video 1). These clusters dissolved over time despite continuous blue-light exposure, suggesting that clustering triggers TRIM37 autodegradation. Consistently, we observed a marked reduction in whole-cell TRIM37 G322V–mNG–CRY2 protein levels 3 h after blue-light exposure (Extended Data Fig. 5d). Proteasome inhibition with MG132 prevented both the time-dependent loss of TRIM37 G322V–mNG–CRY2 clusters and the decline in protein levels observed following blue-light stimulation (Extended Data Fig. 5b–d and Supplementary Video 2). Importantly, we also observed the emergence of HMW TRIM37 G322V–mNG–CRY2 in the presence of MG132 and blue light (Extended Data Fig. 5d, lane 5 versus lane 4), implying that CRY2-induced clustering triggers TRIM37 oligomerization and subsequent autodegradation through the proteasome pathway.

Having shown that TRIM37 can be activated through clustering independent of substrate binding, we extended our investigation to determine the effect of substrate-driven clustering on TRIM37 activity. We fused mCherry–CRY2 to the C-terminal unstructured

Fig. 7 | Optogenetic clustering of centrosomal substrates triggers recognition and activation of TRIM37. a, Left: schematic depicts the blue-light-triggered optogenetic system designed to cluster TRIM37's cognate centrosomal substrates, enabling the investigation of TRIM37 recognition and activation requirements. Right: schematic of constructs used in the optogenetic experiments, including mNG-tagged TRIM37 for visualizing recruitment to centrosomal substrates, mCherry–CRY2–Centrobin$^{567–836}$ and an mCherry–CRY2 control. **b**, Representative time-lapse images of RPE-1 *TRIM37*$^{-/-}$ cells integrated with optogenetic constructs detailed in **a**, incubated with or without doxycycline, in the absence or presence of blue light. Timestamps indicate minutes after blue-light exposure. Data are representative of $n = 3$ biological replicates. Scale bars, 10 µm. **c**, Quantification of mCherry fluorescence intensity from **b**, with each condition comprising >30 cells. Data represent the mean ± s.d. **d**, RPE-1 *TRIM37*$^{-/-}$ cells integrated with optogenetic constructs detailed in **a** were incubated with or without doxycycline in the absence or presence of blue light for 3 h before immunoblotting for the indicated proteins. GAPDH was used as a loading control. Data are representative of $n = 3$ biological replicates. **e**, Representative time-lapse images of RPE-1 *TRIM37*$^{-/-}$ cells integrated with optogenetic constructs and coexpressing different TRIM37 mutants with or without MG132 (10 µM) in the absence or presence of blue light. Timestamps indicate minutes after blue-light exposure. Data are representative of $n = 3$ biological replicates. Scale bars, 10 µm. **f**, Quantification of mCherry fluorescence intensity from **e**, with each condition comprising >30 cells. Data represent the mean ± s.d. **g**, RPE-1 *TRIM37*$^{-/-}$ cells expressing indicated optogenetic constructs and different TRIM37 mutants were treated with or without MG132 (10 µM) in the absence or presence of blue light for 3 h before immunoblotting for the indicated proteins. GAPDH was used as a loading control. Data are representative of $n = 3$ biological replicates.

https://doi.org/10.1038/s41594-025-01540-6

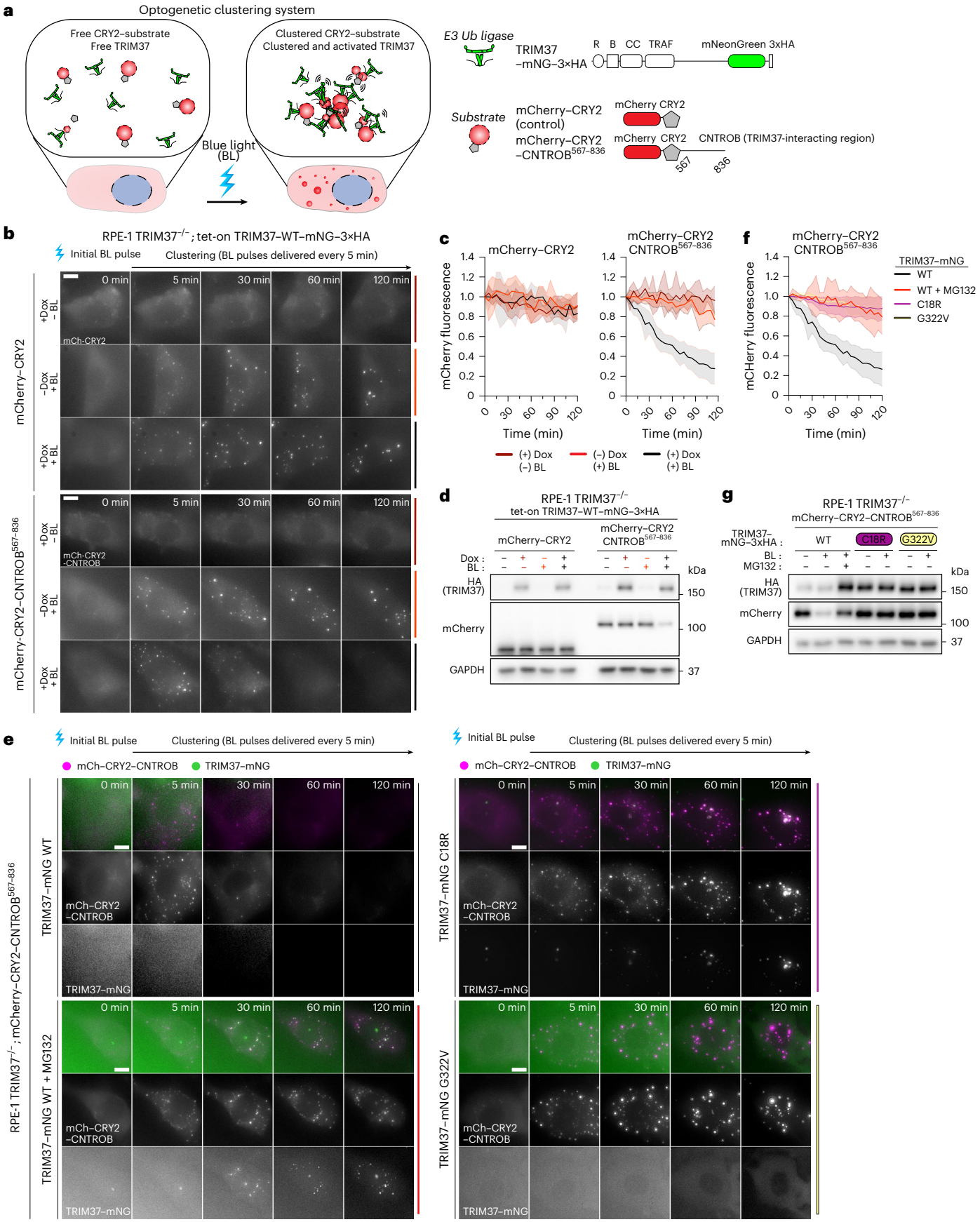

https://doi.org/10.1038/s41594-025-01540-6

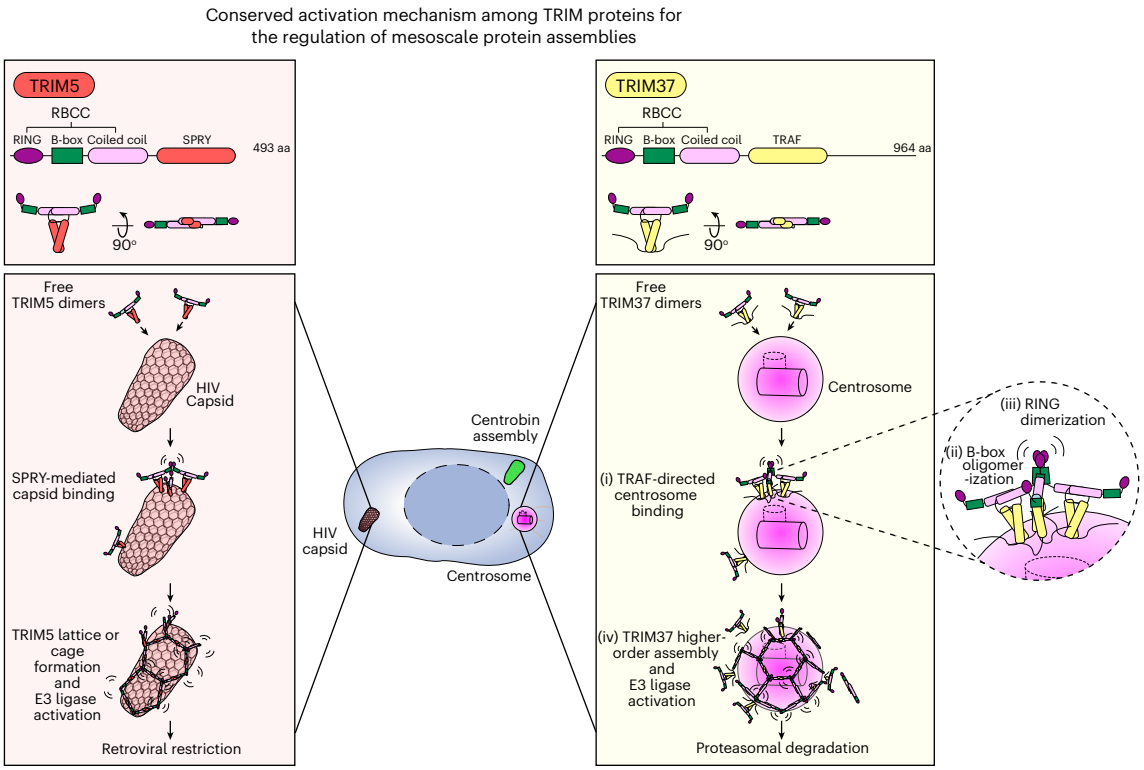

Fig. 8 | TRIM37 regulates MTOC function through substrate-templated higher-order assembly. Model illustrating how TRIM37 regulates MTOCs through substrate-templated higher-order assembly, demonstrated here using centrosomes, highlighting a conserved mechanism reminiscent of TRIM5's role in HIV capsid restriction.

region of Centrobin (residues 567–836) (Fig. 7a), identified as a TRIM37-interacting region. TRIM37 displayed no degradation capability toward mCherry–CRY2 alone, either in a diffuse cytosolic state (without blue light) or a clustered state (with blue light) (Fig. 7b–d and Supplementary Videos 3–5). Illumination with blue light led to the rapid assembly of mCherry–CRY2–Centrobin$^{567–836}$ clusters. Importantly, these clusters dissolved following the induced expression of TRIM37 (Fig. 7b,c and Supplementary Videos 6–8), indicating targeted degradation of the clustered, mCherry-tagged substrate. This was corroborated by a substantial decline in mCherry–CRY2–Centrobin$^{567–836}$ protein levels only in cells expressing TRIM37 and stimulated with blue light (Fig. 7d). These results demonstrate that TRIM37's degradation activity is specifically directed toward substrates that exist in a clustered configuration. The degradation of mCherry–CRY2–Centrobin$^{567–836}$ clusters by TRIM37 required its E3 ligase function for proteasomal degradation and TRAF domain for substrate recruitment. The C18R RING mutant localized to but failed to degrade the mCherry–CRY2–Centrobin$^{567–836}$ clusters, whereas the G322V TRAF mutant was not recruited to the clusters and could not degrade them (Fig. 7e–g and Supplementary Videos 9–12). These findings support a model where TRIM37 is activated through substrate-induced clustering leading to the degradation of the entire TRIM37–substrate complex.

Discussion

Mechanistic dissection of MTOC regulation by TRIM37

In this study, we elucidate the mechanism underlying TRIM37's activation and its role in the regulation of MTOCs. Our findings identify centrosomes, Centrobin assemblies and noncentrosomal PCM foci as platforms for TRIM37 activation. Guided by prior work on TRIM5, we demonstrate that TRIM37 E3 ligase activation occurs following TRAF domain-directed clustering of multiple TRIM37 dimers on its substrate (Fig. 8). Then, upon binding, the oligomerization of TRIM37, mediated by its B-box domain, leads to higher-order structural integrity and increased substrate avidity. Lastly, the interaction of the B-box domains facilitates the dimerization of RING domains from neighboring TRIM37 molecules, culminating in E3 ligase activation and the subsequent degradation of both substrate and TRIM37.

The direct coupling of E3 activation to substrate assembly state allows TRIM37 to discriminate between soluble monomeric proteins and those organized into higher-order structures (Fig. 7). This strategy ensures that TRIM37's regulatory activities are confined to functional MTOCs while preserving a pool of centrosomal building blocks. Notably, we previously showed that TRIM37 abundance is cell cycle regulated, with its levels decreasing in G2 and mitosis[24]—a timing coinciding with PCM expansion and centrosome maturation. The downregulation of TRIM37 levels and autodegradation along with its substrates may constrain the degradative capacity of TRIM37 to avoid complete turnover of centrosome-associated PCM (Figs. 5 and 7 and Extended Data Fig. 5). Additional mechanisms might shield centrosome-incorporated proteins from TRIM37-mediated turnover, ensuring centrosome homeostasis. Such protection could involve kinases driving PCM expansion or deubiquitinases stabilizing centrosomal components. Ultimately, TRIM37's suppression of ncMTOCs reinforces the centrosome's exclusive role during cell division, thereby safeguarding mitotic fidelity.

While it is clear that TRIM37 uses its TRAF domain to localize to and target MTOC structures, how it achieves substrate-specific recognition remains an open question. Complementary findings from Bellaart et al. demonstrate that the TRIM37 TRAF domain binds specific peptide motifs in Centrobin's C-terminal unstructured region[45]. However, these motifs are not apparent in CEP192, suggesting that TRIM37 may rely on distinct mechanisms to recognize and target different substrates. Whether degradation requires the direct binding of TRIM37 to a substrate or occurs collaterally for proteins in close spatial proximity to active TRIM37 remains to be resolved. We favor a model in which specific substrates, such as CEP192 or Centrobin, serve as anchors that recruit and activate TRIM37 at MTOCs, allowing the proximity-induced degradation of proteins. This localization-driven

mechanism conceptually parallels TRIM21, which ubiquitinates and degrades all antibody-bound proteins in its vicinity[46]. Such a model could reconcile TRIM37's ability to mediate broad degradation of MTOC assemblies while remaining anchored to specific substrates through its TRAF domain.

Pathological and therapeutic insights

Our TRIM37 activation model provides a framework for understanding its role in two human conditions associated with centrosome dysfunction. We demonstrate how MUL mutations in *TRIM37* compromise its E3 ligase functionality, giving rise to the formation of pathological Centrobin-scaffolded assemblies. Specifically, the G322V mutation in the TRAF domain prevents substrate engagement necessary for TRIM37's assembly-driven activation, while the C109S mutation in the B-box domain impairs its oligomerization capability.

In cancers characterized by 17q23 amplification, TRIM37 overexpression impedes the assembly of PCM foci that are critical for cells undergoing acentrosomal mitosis[24,25]. This vulnerability underpins an ongoing phase 1 clinical trial (NCT06232408) using a PLK4 inhibitor to induce centrosome loss for cancer killing. Our optogenetic experiments provide additional insight into this synthetic lethal interaction, revealing that the coalescence of centrosomal proteins triggers TRIM37 activation and rapid degradation of these foci (Fig. 7). Consistently, mutations in the B-box that impair TRIM37 oligomerization dramatically reduced the sensitivity of 17q23-amplified cancer cells to PLK4 inhibitor treatment (Extended Data Fig. 4). Additionally, we show that TRIM37's presence at the centrosome is obscured by its autodegradation (Fig. 5). This has implications for patient stratification strategies that leverage TRIM37 overexpression as a biomarker to identify tumors susceptible to PLK4 inhibition. Our data indicate that assessing mRNA expression or total protein detection should be prioritized over immunohistochemistry protocols when evaluating TRIM37 expression levels.

Unified paradigm of mesoscale assembly regulation by TRIMs

Our work highlights that members of the TRIM protein family with the core RBCC domain architecture deploy an evolutionarily conserved strategy for substrate regulation. The acquisition of the TRAF domain[26]—absent in other TRIM proteins—marks a key event that enables the recognition and regulation of centrosome substrates in higher-order configurations[47–50], thus establishing TRIM37 as the principal MTOC regulator within the TRIM superfamily. While this role diverges from the classical antiviral functions ascribed to TRIM proteins such as TRIM5 and TRIM21 (refs. 29,51), our findings suggest a unifying paradigm in which TRIM proteins regulate a spectrum of higher-order assemblies, ranging from extrinsic viral entities to intrinsic cellular structures (Figs. 3 and 8). Echoing its antiviral relatives, we consider TRIM37 as a 'restriction factor' for ncMTOCs. This concept is complemented by the recently identified role of TRIM11 in mitigating Tau aggregation in Alzheimer disease[52], where we speculate that the assembly of Tau fibrils may act as the trigger for TRIM11-mediated degradation. These insights could lay the groundwork for developing TRIM-based proteolysis-targeting chimera strategies that selectively target pathological assemblies while sparing monomeric proteins.

Online content

Any methods, additional references, Nature Portfolio reporting summaries, source data, extended data, supplementary information, acknowledgements, peer review information; details of author contributions and competing interests; and statements of data and code availability are available at https://doi.org/10.1038/s41594-025-01540-6.

References

1. Conduit, P. T., Wainman, A. & Raff, J. W. Centrosome function and assembly in animal cells. *Nat. Rev. Mol. Cell Biol.* **16**, 611–624 (2015).
2. Gould, R. R. & Borisy, G. G. The pericentriolar material in Chinese hamster ovary cells nucleates microtubule formation. *J. Cell Biol.* **73**, 601–615 (1977).
3. Schnackenberg, B. J., Khodjakov, A., Rieder, C. L. & Palazzo, R. E. The disassembly and reassembly of functional centrosomes in vitro. *Proc. Natl Acad. Sci. USA* **95**, 9295–9300 (1998).
4. Mennella, V., Agard, D. A., Huang, B. & Pelletier, L. Amorphous no more: subdiffraction view of the pericentriolar material architecture. *Trends Cell Biol.* **24**, 188–197 (2014).
5. Woodruff, J. B., Wueseke, O. & Hyman, A. A.Pericentriolar material structure and dynamics. *Philos. Trans. R. Soc. Lond. B Biol. Sci.* **369**, 20130459 (2014).
6. Nigg, E. A. & Holland, A. J. Once and only once: mechanisms of centriole duplication and their deregulation in disease. *Nat. Rev. Mol. Cell Biol.* **19**, 297–312 (2018).
7. Godinho, S. A. & Pellman, D.Causes and consequences of centrosome abnormalities in cancer. *Philos. Trans. R. Soc. Lond. B Biol. Sci.* **369**, 20130467 (2014).
8. Phan, T. P. & Holland, A. J. Time is of the essence: the molecular mechanisms of primary microcephaly. *Genes Dev.* **35**, 1551–1578 (2021).
9. Sanchez, A. D. & Feldman, J. L. Microtubule-organizing centers: from the centrosome to non-centrosomal sites. *Curr. Opin. Cell Biol.* **44**, 93–101 (2017).
10. Li, J. et al. Neurl4, a novel daughter centriole protein, prevents formation of ectopic microtubule organizing centres. *EMBO Rep.* **13**, 547–553 (2012).
11. Shiratsuchi, G., Takaoka, K., Ashikawa, T., Hamada, H. & Kitagawa, D. RBM14 prevents assembly of centriolar protein complexes and maintains mitotic spindle integrity. *EMBO J.* **34**, 97–114 (2015).
12. Ozato, K., Shin, D. M., Chang, T. H. & Morse, H. C. 3rdTRIM family proteins and their emerging roles in innate immunity. *Nat. Rev. Immunol.* **8**, 849–860 (2008).
13. Avela, K. et al. Gene encoding a new RING–B-box–coiled-coil protein is mutated in Mulibrey nanism. *Nat. Genet.* **25**, 298–301 (2000).
14. Kallijarvi, J., Avela, K., Lipsanen-Nyman, M., Ulmanen, I. & Lehesjoki, A. E. The *TRIM37* gene encodes a peroxisomal RING–B-box–coiled-coil protein: classification of Mulibrey nanism as a new peroxisomal disorder. *Am. J. Hum. Genet* **70**, 1215–1228 (2002).
15. Kettunen, K. M. et al. *Trim37*-deficient mice recapitulate several features of the multi-organ disorder Mulibrey nanism. *Biol. Open* **5**, 584–595 (2016).
16. Balestra, F. R., Strnad, P., Fluckiger, I. & Gonczy, P. Discovering regulators of centriole biogenesis through siRNA-based functional genomics in human cells. *Dev. Cell* **25**, 555–571 (2013).
17. Dominguez-Calvo, A., Gonczy, P., Holland, A. J. & Balestra, F. R. TRIM37: a critical orchestrator of centrosome function. *Cell Cycle* **20**, 2443–2451 (2021).
18. Meitinger, F. et al. 53BP1 and USP28 mediate p53 activation and G1 arrest after centrosome loss or extended mitotic duration. *J. Cell Biol.* **214**, 155–166 (2016).
19. Meitinger, F. et al. TRIM37 prevents formation of condensate-organized ectopic spindle poles to ensure mitotic fidelity. *J. Cell Biol.* **220**, e202010180 (2021).
20. Balestra, F. R. et al. TRIM37 prevents formation of centriolar protein assemblies by regulating Centrobin. *eLife* **10**, e62640 (2021).
21. Andersen, C. L. et al. High-throughput copy number analysis of 17q23 in 3520 tissue specimens by fluorescence in situ hybridization to tissue microarrays. *Am. J. Pathol.* **161**, 73–79 (2002).

22. Lastowska, M. et al. Gain of chromosome arm 17q predicts unfavourable outcome in neuroblastoma patients. *Eur. J. Cancer* **33**, 1627–1633 (1997).
23. Sinclair, C. S., Rowley, M., Naderi, A. & Couch, F. J. The 17q23 amplicon and breast cancer. *Breast Cancer Res. Treat.* **78**, 313–322 (2003).
24. Yeow, Z. Y. et al. Targeting TRIM37-driven centrosome dysfunction in 17q23-amplified breast cancer. *Nature* **585**, 447–452 (2020).
25. Meitinger, F. et al. TRIM37 controls cancer-specific vulnerability to PLK4 inhibition. *Nature* **585**, 440–446 (2020).
26. Meroni, G. & Diez-Roux, G. TRIM/RBCC, a novel class of 'single protein RING finger' E3 ubiquitin ligases. *Bioessays* **27**, 1147–1157 (2005).
27. Hamalainen, R. H. et al. Novel mutations in the *TRIM37* gene in Mulibrey nanism. *Hum. Mutat.* **23**, 522 (2004).
28. Hamalainen, R. H. et al. Wilms' tumor and novel *TRIM37* mutations in an Australian patient with Mulibrey nanism. *Clin. Genet.* **70**, 473–479 (2006).
29. Ganser-Pornillos, B. K. & Pornillos, O. Restriction of HIV-1 and other retroviruses by TRIM5. *Nat. Rev. Microbiol.* **17**, 546–556 (2019).
30. Sanchez, J. G. et al. The tripartite motif coiled-coil is an elongated antiparallel hairpin dimer. *Proc. Natl Acad. Sci. USA* **111**, 2494–2499 (2014).
31. Goldstone, D. C. et al. Structural studies of postentry restriction factors reveal antiparallel dimers that enable avid binding to the HIV-1 capsid lattice. *Proc. Natl Acad. Sci. USA* **111**, 9609–9614 (2014).
32. Li, Y. L. et al. Primate TRIM5 proteins form hexagonal nets on HIV-1 capsids. *eLife* **5**, e16269 (2016).
33. Yudina, Z. et al. RING dimerization links higher-order assembly of TRIM5α to synthesis of K63-linked polyubiquitin. *Cell Rep.* **12**, 788–797 (2015).
34. Jumper, J. et al. Highly accurate protein structure prediction with AlphaFold. *Nature* **596**, 583–589 (2021).
35. Gheiratmand, L. et al. Spatial and proteomic profiling reveals centrosome-independent features of centriolar satellites. *EMBO J.* **38**, e101109 (2019).
36. Gupta, G. D. et al. A dynamic protein interaction landscape of the human centrosome–cilium interface. *Cell* **163**, 1484–1499 (2015).
37. Diaz-Griffero, F. et al. A B-box 2 surface patch important for TRIM5α self-association, capsid binding avidity, and retrovirus restriction. *J. Virol.* **83**, 10737–10751 (2009).
38. Wagner, J. M. et al. Mechanism of B-box 2 domain-mediated higher-order assembly of the retroviral restriction factor TRIM5α. *eLife* **5**, e16309 (2016).
39. Massiah, M. A. Zinc-binding B-box domains with RING folds serve critical roles in the protein ubiquitination pathways in plants and animals. In *Ubiquitin Proteasome System* (ed. Summers, M.) (IntechOpen, 2019).
40. Reymond, A. et al. The tripartite motif family identifies cell compartments. *EMBO J.* **20**, 2140–2151 (2001).
41. Li, X. & Sodroski, J. The TRIM5α B-box 2 domain promotes cooperative binding to the retroviral capsid by mediating higher-order self-association. *J. Virol.* **82**, 11495–11502 (2008).
42. Fletcher, A. J. et al. Trivalent RING assembly on retroviral capsids activates TRIM5 ubiquitination and innate immune signaling. *Cell Host Microbe* **24**, 761–775 (2018).
43. Zeng, J. et al. Target-induced clustering activates Trim-Away of pathogens and proteins. *Nat. Struct. Mol. Biol.* **28**, 278–289 (2021).
44. Park, H. et al. Optogenetic protein clustering through fluorescent protein tagging and extension of CRY2. *Nat. Commun.* **8**, 30 (2017).
45. Bellaart, A. et al. TRIM37 prevents ectopic spindle pole assembly by peptide motif recognition and substrate-dependent oligomerization. *Nat. Struct. Mol. Biol.* (in the press).
46. Kiss, L. et al. Trim-Away ubiquitinates and degrades lysine-less and N-terminally acetylated substrates. *Nat. Commun.* **14**, 2160 (2023).
47. Fu, J. & Glover, D. M. Structured illumination of the interface between centriole and peri-centriolar material. *Open Biol.* **2**, 120104 (2012).
48. Lawo, S., Hasegan, M., Gupta, G. D. & Pelletier, L. Subdiffraction imaging of centrosomes reveals higher-order organizational features of pericentriolar material. *Nat. Cell Biol.* **14**, 1148–1158 (2012).
49. Mennella, V. et al. Subdiffraction-resolution fluorescence microscopy reveals a domain of the centrosome critical for pericentriolar material organization. *Nat. Cell Biol.* **14**, 1159–1168 (2012).
50. Sonnen, K. F., Schermelleh, L., Leonhardt, H. & Nigg, E. A. 3D-structured illumination microscopy provides novel insight into architecture of human centrosomes. *Biol. Open* **1**, 965–976 (2012).
51. Foss, S. et al. TRIM21—from intracellular immunity to therapy. *Front. Immunol.* **10**, 2049 (2019).
52. Zhang, Z. Y. et al. TRIM11 protects against tauopathies and is down-regulated in Alzheimer's disease. *Science* **381**, eadd6696 (2023).

Methods

Cell lines and culture conditions

hTERT RPE-1 and MCF-7 cells were grown in DMEM (Corning Cellgro) containing 10% FBS (Sigma), 100 U per ml penicillin, 100 U per ml streptomycin and 2 mM L-glutamine. All cell lines were maintained at 37 °C in a 5% CO_2 atmosphere with 21% oxygen and routinely checked for mycoplasma contamination.

Gene targeting and stable cell lines

To generate CRISPR–Cas9-mediated KO lines, the single guide RNA targeting *TRIM37* (*TRIM37Δ*, 5′-CTCCCCAAAGTGCACACTGA-3′) was cloned into the PX459 vector (Addgene, 62988) containing a puromycin resistance cassette. Cells were transiently transfected (Lipofectamine LTX, Thermo Fisher Scientific) with the PX459 plasmid and positive selection of transfected cells was performed 2 days after transfection with 2.0 μg ml^{-1} puromycin. Monoclonal cell lines were isolated by limiting dilution. The presence of gene-disrupting insertions or deletions (indels) in edited cell lines was confirmed by Sanger sequencing and analyzed using Tracking of Indels by Decomposition (https://tide.nki.nl/)[53]; the ablation of protein production was assessed by immunoblotting.

To generate TRIM37-overexpressing RPE-1 cell lines, the *TRIM37* open reading frame (ORF) was cloned into a tet-inducible lentiviral vector containing a C-terminal 3×HA tag. The C18R, C109S and G322V mutations were introduced using PCR-directed mutagenesis and subsequently verified by Sanger sequencing. TRIM37 ΔB-box (residues 91–131 deleted), TRIM37 ΔTRAF (residues 274–448 deleted) and miniTRIM37 (residues 459–964 deleted) were constructed by Gibson assembly and verified by Sanger sequencing. Lentiviral particles were produced as described below. Cells were transduced and stable polyclonal populations of cells were selected and maintained in the presence of 1.0 μg ml^{-1} puromycin.

To generate RPE-1 cell lines expressing TRIM5 WT or chimera, the *TRIM5* ORF (Addgene, 79066) was PCR-amplified and cloned into a tet-inducible lentiviral vector containing a C-terminal 3×HA tag. The TRIM5–TRAF chimera was engineered by replacing the SPRY domain (residues 303–493) with TRIM37's TRAF domain (residues 274–448) by Gibson assembly, with the constructs verified by Sanger sequencing. Lentiviral particles were produced as described below. Cells were transduced and stable polyclonal populations of cells were selected and maintained in the presence of 1.0 μg ml^{-1} puromycin.

To generate cell lines expressing mCherry–CRY2 variants, the sequence encoding mCherry–CRY2clust (Addgene, 105624) was PCR-amplified. This construct, either fused with the C-terminal region of Centrobin (residues 567–836) or alone, was then incorporated by Gibson assembly into a constitutive lentiviral vector that included blasticidin resistance. Lentiviral particles were produced as described below. RPE-1 $TRIM37^{-/-}$ cells engineered with tet-inducible TRIM37–mNG were transduced and stable polyclonal populations were selected and maintained in the presence of 30.0 μg ml^{-1} blasticidin.

To generate RPE-1 and MCF-7 cell lines with targeted edits to the endogenous *TRIM37* loci (C18R and C109S, respectively), a CRISPR–Cas9 knock-in (KI) strategy was used as previously described[54]. Specifically, Alt-R CRISPR RNAs (crRNAs) targeting *TRIM37* (C18R, 5′-UCAUUUGUAUGGAGAAAUUGGUUUUAGAGCUAUGCU-3′; C109S, 5′-CUCCCCAAAGUGCACACUGAGUUUUAGAGCUAUGCU-3′; Integrated DNA Technologies) were annealed with *trans*-activating crRNA (Integrated DNA Technologies) and subsequently combined with recombinant Alt-R S.p. Cas9 nuclease V3 (Integrated DNA Technologies). The assembled ribonucleoprotein complexes and corresponding single-stranded DNA homology templates (C18R, 5′-CTTGCCTTTTACTCTTGATTCAGTAGCCTAAACTGGTGGACCTTACATCTTTTACTGTTTTCAGAGCATTGCTGAGGTTTTCCGATGTTTCATCCGTATGGAGAAATTGCGCGATGCACGCCTGTGTCCTCATTGCTCCAAACTGTGTTG-3′; C109S, 5′-TCCAATTTAATTTATAACTTCATTTTCTTTTCATAATGTATAGATGTGAAAATCACCATGAAAAACTTAGTGTATTTTGCTGGACTTCTAAGAAGTGTATCTGCCACCAATGTGCACTTTGGGGAGGAATGGTGAGCAGAACAAATTCAG-3′, Integrated DNA Technologies) were nucleofected into cells using the 4D-Nucleofector X unit (Lonza) following the prescribed protocols: RPE-1, EA-104 program, P3 Buffer; MCF-7, EN-130 program, SE buffer. After electroporation, cells were treated with 1 μM NU7441 (Selleck Chemicals) for 48 h to enhance homology-directed repair efficacy. Monoclonal cell lines were isolated by limiting dilution, with the specific gene edits confirmed by Sanger sequencing.

RNA interference

Short hairpin RNAs (shRNAs) targeting *TRIM37* (TRIM37-1, 5′-TCGAGAATATGATGCTGTG-3′) were cloned into the pGIPz (Thermo Fisher Scientific) vector. Stable shRNA-mediated KD cell lines were generated by lentivirus-mediated transduction. Polyclonal populations of cells were subsequently selected and maintained in the presence of puromycin (1.0 μg ml^{-1}). KD efficiency was assessed by immunoblotting.

Lentiviral production and transduction

Lentiviral expression vectors were cotransfected into 293FT cells with the lentiviral packaging plasmids psPAX2 and pMD2.G (Addgene, 12260 and 12259). Briefly, 3×10^6 293FT cells were seeded into a poly(L-lysine)-coated 10-cm culture dish the day before transfection. For each 10-cm dish, the following DNAs were diluted in 0.6 ml of OptiMEM (Thermo Fisher Scientific): 4.5 μg of lentiviral vector, 6 μg of psPAX2 and 1.5 μg of pMD2.G. Separately, 72 μl of 1 μg $μl^{-1}$ 25-kDa polyethyleneimine (PEI; Sigma) was diluted into 1.2 ml of OptiMEM, briefly vortexed and incubated at room temperature for 5 min. After incubation, the DNA and PEI mixtures were combined, briefly vortexed and incubated at room temperature for 20 min. During this incubation, the culture medium was replaced with 17 ml of prewarmed DMEM + 1% FBS. The transfection mixture was then added dropwise to the 10-cm dish. Viral particles were isolated 48 h after the medium change and filtered through a 0.45-μm PVDF syringe filter. The filtered supernatant was either concentrated in 100-kDa Amicon Ultra centrifugal filter units (Millipore) or used directly to infect cells. Aliquots were snap-frozen and stored at −80 °C. For transduction, lentiviral particles were diluted in complete growth medium supplemented with 10 μg ml^{-1} polybrene (Sigma) and added to cells.

Chemical inhibitors

MG132 (Sigma) was dissolved in DMSO and used at a final concentration of 10 μM. Nocodazole (Selleck Chemicals) was dissolved in DMSO and used at a final concentration of 3.3 μM. Centrinone (Tocris Bioscience) was dissolved in DMSO and used at a final concentration of 250 nM.

Structural modeling and sequence alignment

The structure of monomeric TRIM37 (UniProt O94762) was obtained from the AlphaFold Protein Structure Database[55]. Dimerization of TRIM37 (residues 1–448) was modeled using AlphaFold-Multimer on ColabFold (version 1.5.5)[56,57] with default settings. Of the five models generated, the one with the highest AlphaFold-predicted template modeling score was selected for this study. Structural visualizations were created with UCSF ChimeraX (version 1.6.1)[58]. Alignment of the B-box domains of TRIM5 (rhesus macaque, UniProt Q0PF16; human, UniProt Q9C035) and TRIM37 (human, UniProt O94762) was conducted using Jalview (version 2.11.4.1)[59].

Biotin identification sample preparation, mass spectrometry and data analysis

To generate cell lines for biotin identification (BioID), puro-sensitive RPE-1 cells were transduced with lentivirus containing tet-inducible miniTurbo control or various miniTurbo–TRIM37 constructs. After

48 h, cells were selected in 2.0 µg ml^{-1} puromycin for 2 days followed by expansion into two 15-cm dishes. Then, 6 h before biotin labeling, 1 µg ml^{-1} doxycycline was added to induce expression of miniTurbo constructs. The culture medium was then supplemented with 250 µM D-biotin (P212121; prepared as 250 mM stock in DMSO) to initiate labeling of proximity interactors. Samples were collected after 4 h of biotin labeling, transferred to 15-ml conical tubes and rinsed four times with ice-cold PBS to eliminate excess biotin. Cell pellets were lysed in ~1.5 ml of lysis buffer (all buffer recipes were previously published[60]) by gentle pipetting followed by sonication. Lysates were then clarified by centrifugation at 16,000*g* (15 min, 4 °C). Biotinylated proteins were enriched by incubating 50 µl of streptavidin agarose bead resin (Pierce) with the lysates, rotating overnight at 4 °C. Beads were then washed for 10 min each with a series of four wash buffers of decreasing detergent concentrations followed by two final washes in 50 mM ammonium bicarbonate and then resuspended in ~60 µl of the same buffer before freezing for mass spectrometry (MS).

For MS preparation, proteins were reduced with 1.75 µl of 15 mg ml^{-1} DTT in 10 mM TEAB, shaking at 56 °C for 50 min. Samples were then cooled to room temperature, the pH was adjusted to 8 with 500 mM TEAB buffer and the sample was alkylated with 1.8 µl of 36 mg ml^{-1} iodoacetamide in 100 mM TEAB for 20 min in the dark. Proteolysis was performed by adding 20 ng µl^{-1} trypsin (Promega) and incubating at 37 °C overnight. Supernatants were collected and beads were washed with 0.1× TFA three times, with washes added to the supernatant. The pH was adjusted to acidic range and peptides were desalted on u-HLB Oasis plates, eluted with 60% acetonitrile + 0.1% TFA and dried. A 10% aliquot of desalted peptides was analyzed on a Nano liquid chromatograph with MS/MS on a Q Exactive Plus (Thermo Fisher Scientific) in Fourier transform mode. MS/MS data were processed with Mascot through PD2.2 against RefSeq2017_83 human species database and a database containing small enzymes and standards containing using the FilesRC option, with a mass tolerance of 3 ppm on precursors and 0.01 Da on fragments, while annotating variable modifications such as oxidation on M, carbamidomethyl on C and deamidation on NQ, with and without biotin K. The resulting Mascot.dat files were compiled in Scaffold and processed in PD2.2 to identify peptides and proteins using Percolator as a PSM validator.

Protein hits identified exclusively in miniTurbo–TRIM37 BioID and those whose spectral counts in miniTurbo–TRIM37 (WT and C18R) BioID were at least twofold greater than those of mTurbo alone (control) were considered as candidates for TRIM37 interaction. A second criterion was applied whereby hits whose spectral counts in miniTurbo–TRIM37 (WT and C18R) BioID were twofold greater than those of miniTurbo–TRIM37 (G322V) were identified as TRAF-specific interactors. Additionally, the minimum spectral count for inclusion was set to two and common contaminants listed on the CRAPome database[61] were excluded. The filtered list of BioID hits was annotated with GO terms through the Panther classification system[62] and analyzed using the statistical overrepresentation test (binomial) to derive *P* values[63]. Visualization of data was performed using the dot plot generator from ProHits-viz[64].

Antibody techniques

For immunoblot analyses, protein samples were resolved by SDS–PAGE on pre-cast NuPAGE gels (1.0 mm 4–12% Bis–Tris or 1.5 mm 3–8% Tris–acetate for HMW TRIM37; Invitrogen) with molecular weight ladders (PageRuler Plus or HiMark prestained protein standard for HMW TRIM37; Invitrogen). Following electrophoresis, proteins were transferred onto nitrocellulose membranes using a Mini Trans-Blot Cell (BioRad) wet transfer system and subsequently probed with the following primary antibodies: anti-TRIM37 (rabbit; Bethyl, A301-174A; 1:1,000), anti-HA (rat; Roche, ROAHAHA; 1:1,000), anti-β-actin (mouse; Santa Cruz Biotechnology, sc-4778; 1:1,000), anti-CEP192 (rabbit, raised against CEP192 residues 1–211, homemade[24]; 1:1,000), anti-Centrobin (rabbit; Atlas Antibodies, HPA023319; 1:1,000), anti-SAS6 (mouse; Santa Cruz Biotechnology, sc-81431; 1:1,000), anti-vinculin (mouse; Santa Cruz Biotechnology, sc-73614; 1:1,000), anti-GAPDH (mouse; Santa Cruz Biotechnology, sc-47724; 1:1,000), anti-TRIM37 (rabbit; Cell Signaling, 96167; 1:1,000; Fig. 5e–g) and anti-mCherry (rabbit; Abcam, ab167453; 1:4,000). Detection was performed using horseradish-peroxidase-conjugated secondary antibodies: anti-mouse (horse; Cell Signaling, 7076; 1:1,000), anti-rat (goat; Cell Signaling, 7077; 1:1,000), anti-rabbit (goat; Cell Signaling, 7074, 1:1,000), and anti-streptavidin (Cell Signaling, 3999; 1:1,500), with SuperSignal West Pico PLUS or Femto maximum chemiluminescence substrate (Thermo Fisher Scientific). Signals were visualized and acquired using a Genesys G:Box Chemi-XX6 system (Syngene).

For immunofluorescence, cells were cultured on 12-mm glass coverslips and fixed for 8 min in 100% ice-cold methanol at −20 °C. Cells were blocked in 2.5% FBS, 200 mM glycine and 0.1% Triton X-100 in PBS for 1 h. Antibody incubations were conducted in the blocking solution for 1 h. DNA was stained with DAPI and cells were mounted in ProLong Gold Antifade (Invitrogen). Staining was performed with the following primary antibodies: anti-HA (rat; Roche, ROAHAHA; 1:500), CEP192–Cy5 (directly labeled goat, raised against CEP192 residues 1–211, homemade; 1:1,000), anti-Centrobin (rabbit; Atlas Antibodies, HPA023319; 1:1,000), anti-streptavidin–Alexa Fluor 555 (Invitrogen, S32355; 1:1,000), anti-β-tubulin (guinea pig; ABCD Antibodies, ABCD_AA344; 1:4,000), anti-TRIM37 (rabbit; Cell Signaling, 96167; 1:1,000; Fig. 5e–g), anti-Centrin (mouse; Millipore, 04-1624; 1:1,000) and anti-α-tubulin (rat; Invitrogen, MA1-80017; 1:1,000).

Immunofluorescence images were acquired using a DeltaVision Elite system (GE Healthcare) controlling a scientific complementary metal–oxide–semiconductor (CMOS) camera (pco.edge 5.5). Acquisition parameters were controlled by SoftWoRx suite (GE Healthcare). Images were collected at room temperature (25 °C) using an Olympus ×40 (1.35 numerical aperture (NA)), ×60 (1.42 NA) or ×100 (1.4 NA) oil objective at 0.2-µm *z* sections. Images were acquired using Applied Precision immersion oil ($N = 1.516$). For quantitation of signal intensity at the centrosome, deconvolved two-dimensional (2D) maximum intensity projections were saved as 16-bit TIFF images. Signal intensity was determined using ImageJ by drawing a circular region of interest (ROI) around the centriole (ROI S). A larger concentric circle (ROI L) was drawn around ROI S. ROIs S and L were applied to the channel of interest and the signal in ROI S was calculated using the formula $I_S - [(I_L - I_S/A_L - A_S) \times A_S]$, where A is the area and I is the integrated pixel intensity.

Centrosome enrichment assays

Centrosome purification was performed as described previously[65], with some modifications. RPE-1 cells seeded at a density of 2×10^6 cells in 15-cm dishes were treated with 1 µg ml^{-1} doxycycline (Thermo Fisher Scientific) for 18 h to induce TRIM37 protein expression. Before harvest, cells were treated with 3.3 µM nocodazole (Selleck Chemicals) and 5 µg ml^{-1} cytochalasin B (Cayman Chemical) for 1 h and 15 min to depolymerize microtubule and actin networks, thus facilitating the dissociation of centrosomes from the nuclei. Cells were then washed sequentially with ice-cold 1× PBS, 8% sucrose in 0.1× PBS, 8% sucrose in deionized H_2O and Tris-HCl (pH 8.0) containing 0.46 µl ml^{-1} β-mercaptoethanol (β-ME) (Sigma). Lysis was carried out at 4 °C with a 1 mM Tris-HCl buffer (pH 8.0) that included 0.5% IGEPAL CA-630 (Sigma), 0.5 mM $MgCl_2$, 0.1 mM PMSF (Sigma), 0.1 mM *ortho*-vanadate (Sigma), protease and phosphatase cocktail inhibitors (Roche), 0.46 µl ml^{-1} β-ME and 10 U per L Benzonase (MilliporeSigma), with vigorous rocking for 15 min. The whole-cell lysate was initially centrifuged at 2,500*g* (5 min, 4 °C) to isolate the nuclear fraction (pellet). The supernatant was then subjected to ultracentrifugation at 21,100*g* (15 min, 4 °C) to further separate the centrosome-containing fraction (pellet) from the cytosolic fraction.

In vivo crosslinking assays

RPE-1 cells seeded at a density of 9×10^5 cells per well in 12-well plates were treated with 1 μg ml^{-1} doxycycline (Thermo Fisher Scientific) for 16 h to induce TRIM37 protein expression. Crosslinking agents DSS and DSG (Thermo Fisher Scientific) were then prepared as solutions in DMSO and added to the culture medium. After a 12-min incubation at room temperature to facilitate crosslinking, the medium containing crosslinkers was removed and the reaction was quenched by adding a 50 mM Tris-HCl solution (pH 8.0) directly to the wells for an additional 10 min at room temperature. Cell lysates were subsequently harvested, clarified by brief centrifugation at 8,000*g* (5 min, 4 °C) and prepared for immunoblot analysis.

Blue-light-induced CRY2 clustering experiments

Fluorescent RPE-1 cell lines were seeded into μ-Slide four-well or eight-well glass-bottom chamber slides (Ibidi). Cells were treated with 1 μg ml^{-1} doxycycline, with or without MG132, to induce TRIM37 protein expression 1 h before blue-light exposure and were kept in the dark.

Time-lapse imaging was performed using a Zeiss Axio Observer 7 inverted microscope equipped with Slidebook 2024 software (3i—Intelligent, Imaging Innovations), X-Cite NOVEM-L light-emitting diode (LED) laser and filter cubes and a Prime 95B CMOS camera (Teledyne Photometrics) with a ×40 (1.3 NA) plan-apochromat oil immersion objective. During imaging, cell conditions were maintained at 37 °C, 5% CO_2 and 60% relative humidity using a stage-top incubator (Okolab). A 470-nm filter was used to induce CRY2 clustering and simultaneously image TRIM37–mNG, while a 555-nm filter was used for mCherry–CRY2 visualization. Images were captured every 5 min in *z* sections of 14 × 2 μm and integrated fluorescence intensity measurements (ROIs were manually delineated to encompass the full area of each individual cell where clustering occurred) were derived from maximum intensity projected 2D time-lapse images in Fiji. Following background subtraction, fluorescence intensity was normalized to the initial image frame ($t = 0$, before blue-light illumination).

For immunoblot analysis, cells seeded into μ-Slide four-well or eight-well glass-bottom chamber slides (Ibidi) were exposed to blue light using a DR89X blue LED transilluminator (Clare Chemical) controlled by a programmable timed power switch. The exposure regimen involved cycles of 5 s of blue-light exposure ('on') followed by 5 min 'off', continuing over a total duration of 3 h before the cells were harvested.

PLK4i survival assays

MCF-7 cells seeded in triplicate at a density of 1.25×10^4 cells per well in six-well plates were treated with either DMSO (control) or PLK4i (250 nM centrinone) 16 h later. After the indicated number of days, cells were fixed and stained using 0.5% (w/v) crystal violet in 20% (v/v) methanol for 5 min. Excess crystal violet was thoroughly rinsed away with distilled water and plates were dried overnight. For quantification, bound crystal violet was dissolved in 10% (v/v) acetic acid in distilled H_2O and the absorbance of 1:50 dilutions was measured at 595 nm using a Synergy HT microplate reader (BioTek Instruments). The optical density at 595 nm served as a quantitative metric of relative cell growth.

Statistical analysis

GraphPad Prism (version 9) was used for graphing and statistical analyses. Specific statistical methods for each experiment are provided in the figure legends.

Reporting summary

Further information on research design is available in the Nature Portfolio Reporting Summary linked to this article.

Data availability

The BioID MS proteomics data were deposited to the ProteomeXchange Consortium through the PRIDE partner repository under accession number PXD061083. Source data are provided with this paper.

References

53. Brinkman, E. K., Chen, T., Amendola, M. & van Steensel, B. Easy quantitative assessment of genome editing by sequence trace decomposition. *Nucleic Acids Res.* **42**, e168 (2014).
54. Ghetti, S. et al. CRISPR/Cas9 ribonucleoprotein-mediated knockin generation in hTERT-RPE1 cells. *STAR Protoc.* **2**, 100407 (2021).
55. Varadi, M. et al. AlphaFold Protein Structure Database in 2024: providing structure coverage for over 214 million protein sequences. *Nucleic Acids Res.* **52**, D368–D375 (2023).
56. Evans, R. et al. Protein complex prediction with AlphaFold-Multimer. Preprint at *bioRxiv* https://doi.org/10.1101/2021.10.04.463034 (2022).
57. Mirdita, M. et al. ColabFold: making protein folding accessible to all. *Nat. Methods* **19**, 679–682 (2022).
58. Meng, E. C. et al. UCSF ChimeraX: tools for structure building and analysis. *Protein Sci.* **32**, e4792 (2023).
59. Waterhouse, A. M., Procter, J. B., Martin, D. M., Clamp, M. & Barton, G. J. Jalview version 2—a multiple sequence alignment editor and analysis workbench. *Bioinformatics* **25**, 1189–1191 (2009).
60. Firat-Karalar, E. N. & Stearns, T. Probing mammalian centrosome structure using BioID proximity-dependent biotinylation. *Methods Cell. Biol.* **129**, 153–170 (2015).
61. Mellacheruvu, D. et al. The CRAPome: a contaminant repository for affinity purification–mass spectrometry data. *Nat. Methods* **10**, 730–736 (2013).
62. Thomas, P. D. et al. PANTHER: making genome-scale phylogenetics accessible to all. *Protein Sci.* **31**, 8–22 (2022).
63. Mi, H. et al. Protocol update for large-scale genome and gene function analysis with the PANTHER classification system (v.14.0). *Nat. Protoc.* **14**, 703–721 (2019).
64. Knight, J. D. R. et al. ProHits-viz: a suite of web tools for visualizing interaction proteomics data. *Nat. Methods* **14**, 645–646 (2017).
65. Shukla, A., Kong, D., Sharma, M., Magidson, V. & Loncarek, J. Plk1 relieves centriole block to reduplication by promoting daughter centriole maturation. *Nat. Commun.* **6**, 8077 (2015).

Acknowledgements

This work was supported by research grants R01GM114119, R01GM133897 and R01CA266199 (to A.J.H) from the National Institutes of Health. M.v.B. was supported by the Queen Mary University of London and by the Biotechnology and Biological Sciences Research Council (BB/X013030/1). We thank M. R. Leung and N. K. Sinha for providing valuable experimental insights.

Author contributions

Z.Y.Y. designed, performed and analyzed the majority of the experiments and prepared the figures. S.S., F.-C.C. and L.Y.X. assisted with the cloning and immunofluorescence analyses. M.v.B. performed the experiments to identify TRIM37-binding regions within Centrobin. Z.Y.Y. and A.J.H. conceptualized the study. A.J.H. supervised the study. Z.Y.Y. and A.J.H. cowrote the paper.

Competing interests

The authors declare no competing interests.

Additional information

Extended data is available for this paper at https://doi.org/10.1038/s41594-025-01540-6.

Supplementary information The online version contains supplementary material available at https://doi.org/10.1038/s41594-025-01540-6.

Correspondence and requests for materials should be addressed to Zhong Y. Yeow or Andrew J. Holland.

Peer review information *Nature Structural & Molecular Biology* thanks the anonymous reviewers for their contribution to the peer review of this work. Peer reviewer reports are available. Primary Handling Editor: Dimitris Typas, in collaboration with the *Nature Structural & Molecular Biology* team.

https://doi.org/10.1038/s41594-025-01540-6

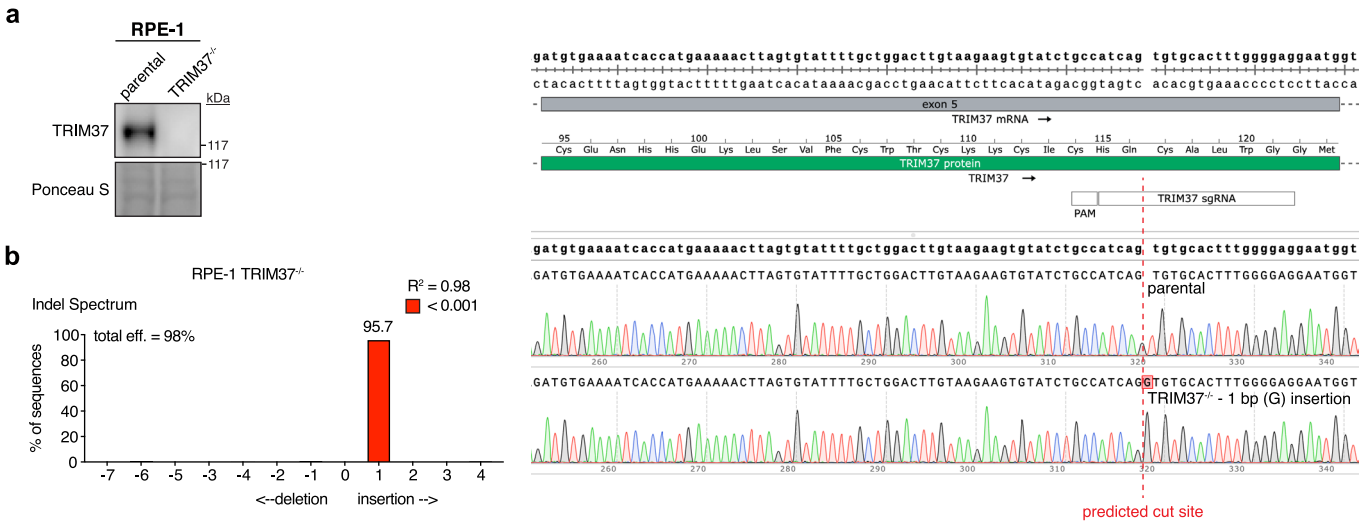

Extended Data Fig. 1 | Effect of TRIM37 mutations on the regulation of the centrosome and Centrobin assemblies. Related to Fig. 1. (**a**) Immunoblot showing TRIM37 protein levels in parental and CRISPR–Cas9 edited RPE-1 *TRIM37*$^{-/-}$ cells. Ponceau-stained blot indicates loading. Representative data; $n = 3$ biological replicates. (**b**) Left, Tracking of Indels by Decomposition (TIDE) analysis histogram reveals a one base pair insertion (+ 1 bp) adjacent to the predicted cut site in the RPE-1 *TRIM37*$^{-/-}$ cell line. Right, representative Sanger sequencing traces used for TIDE analysis, highlighting the +1 bp insertion. (**c**) Representative images of RPE-1 *TRIM37*$^{-/-}$ cells and those expressing the indicated HA-tagged TRIM37 variants. Inset #1 denotes the centrosome, marked by CEP192, and inset #2 denotes the Centrobin assembly, identified by intense Centrobin staining that is non-centrosome localized. Representative data; $n = 3$ biological replicates. Scale bars, 5 µm. (**d**) Schematic representation of TRIM37 HA-tagged domain-specific deletion constructs compared to full-length (FL) protein. (**e**) Immunoblot showing expression levels of FL TRIM37 and the respective deletion mutants in RPE-1 tet-on TRIM37 cells. Ponceau-stained blot indicates loading. Representative data; $n = 3$ biological replicates.

https://doi.org/10.1038/s41594-025-01540-6

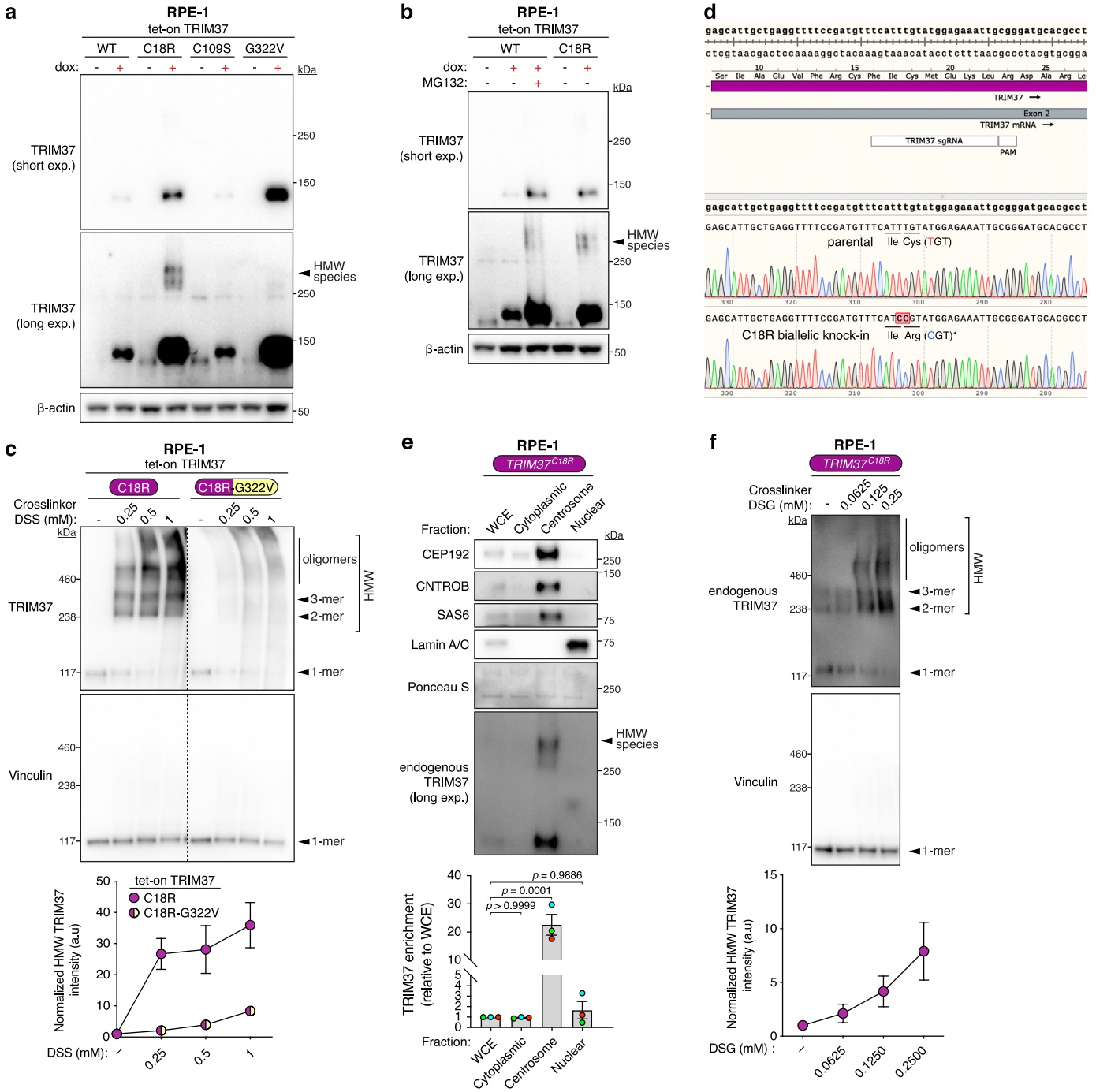

Extended Data Fig. 2 | Characterization of higher molecular weight (HMW) TRIM37 species. Related to Fig. 4. (**a**) Immunoblot showing expression of WT TRIM37 and indicated mutants in RPE-1 tet-on TRIM37 cells. HMW TRIM37 species are prominently formed in the C18R mutant and indicated with an arrow. β-Actin, loading control. Representative data; $n = 3$ biological replicates. (**b**) Same as in (**a**) but with MG132 (10 μM) treatment to achieve proteasomal inhibition and stabilization of WT TRIM37. β-Actin, loading control. Representative data; $n = 3$ biological replicates. (**c**) Top, immunoblot showing detection of HMW TRIM37 species with increasing concentrations of DSS crosslinker. Vinculin is the loading and oligomerization control. Dotted lines indicate separate cropped sections of the same immunoblot. Representative data; $n = 3$ biological replicates. Bottom, Densitometric analysis of normalized HMW TRIM37 intensity upon increasing DSS concentrations relative to DMSO control (− DSS). Mean ± s.e.m. (**d**) Sanger sequencing traces of the *TRIM37* locus in parental and CRISPR–Cas9 edited RPE-1 *TRIM37*^{C18R} cells, highlighting the mutation (TGT > CGT) responsible for the biallelic C18R residue substitution, denoted by an asterisk. (**e**) Top, immunoblot showing endogenous TRIM37 protein levels across the indicated cellular fractions. Validation markers include CEP192, Centrobin, and SAS6 for centrosomal proteins, and Lamin A/C for the nuclear fraction. Ponceau-stained blot indicates loading. Representative data; $n = 3$ biological replicates. WCE, whole-cell extract; exp, exposure. Bottom, Densitometric analysis of endogenous TRIM37 enrichment in indicated fractions relative to WCE. *P* values, one-way ANOVA with post hoc Dunnett's multiple comparisons test to evaluate enrichment of TRIM37 in each cellular fraction relative to WCE. Mean ± s.e.m. (**f**) Top, immunoblot showing detection of various HMW species of endogenous TRIM37 upon treatment with increasing concentrations of DSG crosslinker. Vinculin is the loading and oligomerization control. Representative data; $n = 3$ biological replicates. Bottom, Densitometric analysis of normalized HMW TRIM37 intensity upon increasing DSG concentrations relative to DMSO control (− DSG). Mean ± s.e.m.

https://doi.org/10.1038/s41594-025-01540-6

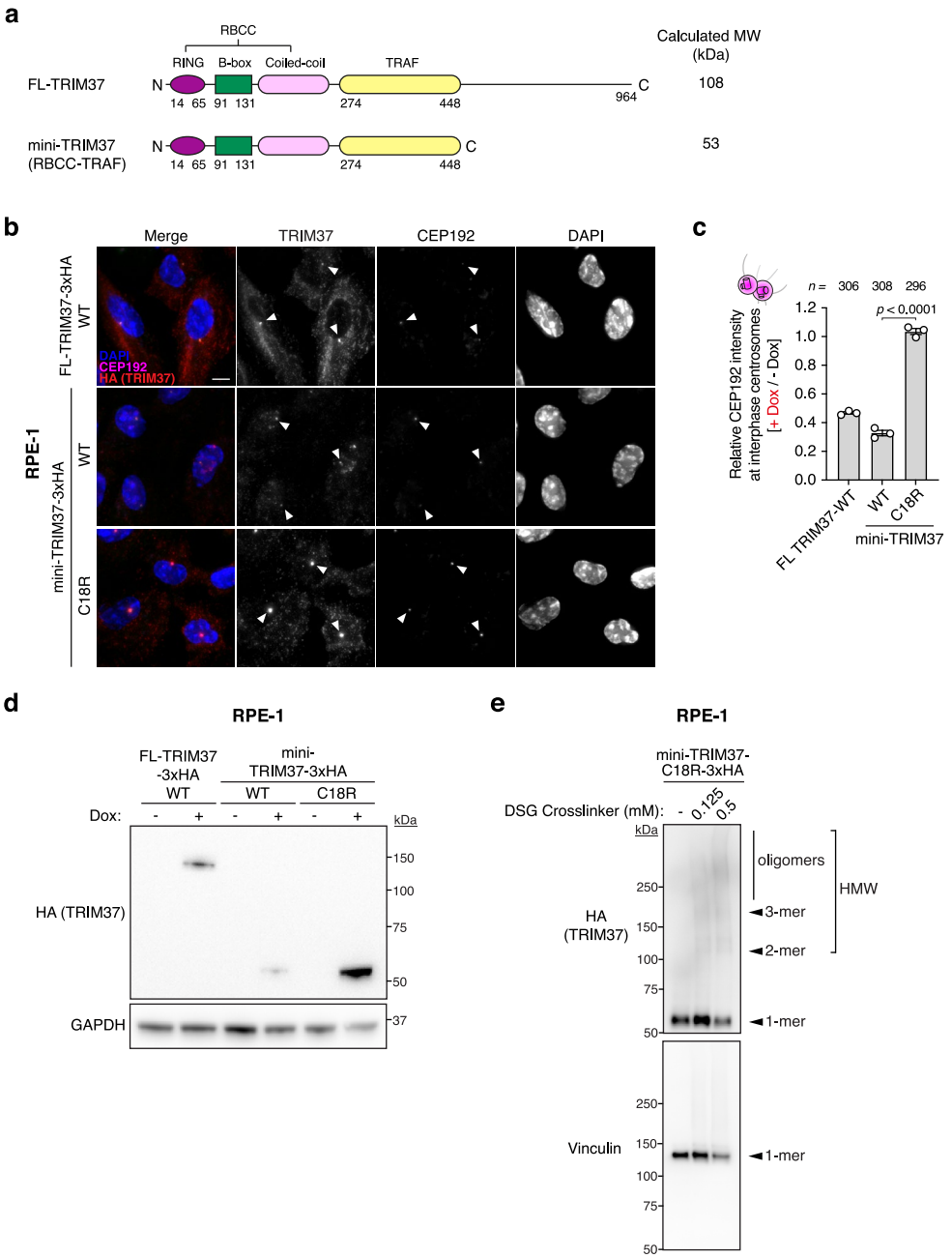

Extended Data Fig. 3 | Defining the minimal TRIM37 domain architecture required for centrosome regulation. a) Schematic of the miniTRIM37 (RBCC-TRAF) construct compared to full-length TRIM37. (**b**) Representative images of the localization and effect of indicated HA-tagged TRIM37 constructs on centrosomal CEP192 levels in RPE-1 tet-on TRIM37 cells. Arrows indicate the positions of centrosomes. Representative data; $n = 3$ biological replicates. Scale bars, 5 µm. (**c**) Quantification of centrosomal CEP192 signal upon doxycycline-induced expression of indicated HA-tagged TRIM37 constructs in RPE-1 tet-on TRIM37 cells from (**b**). $n = 3$ biological replicates, each with >90 cells. *P* values, one-way ANOVA with post hoc Tukey's multiple comparisons test. Mean ± s.e.m. (**d**) Immunoblot showing total protein levels of indicated HA-tagged TRIM37 constructs in RPE-1 tet-on TRIM37 cells from (**b**-**c**). GAPDH, loading control. Representative data; $n = 3$ biological replicates. (**e**) Immunoblot showing detection of various higher molecular weight (HMW) species of miniTRIM37 upon treatment with increasing concentrations of DSG crosslinker. Vinculin is used as a loading and oligomerization control. Representative data; $n = 3$ biological replicates.

https://doi.org/10.1038/s41594-025-01540-6

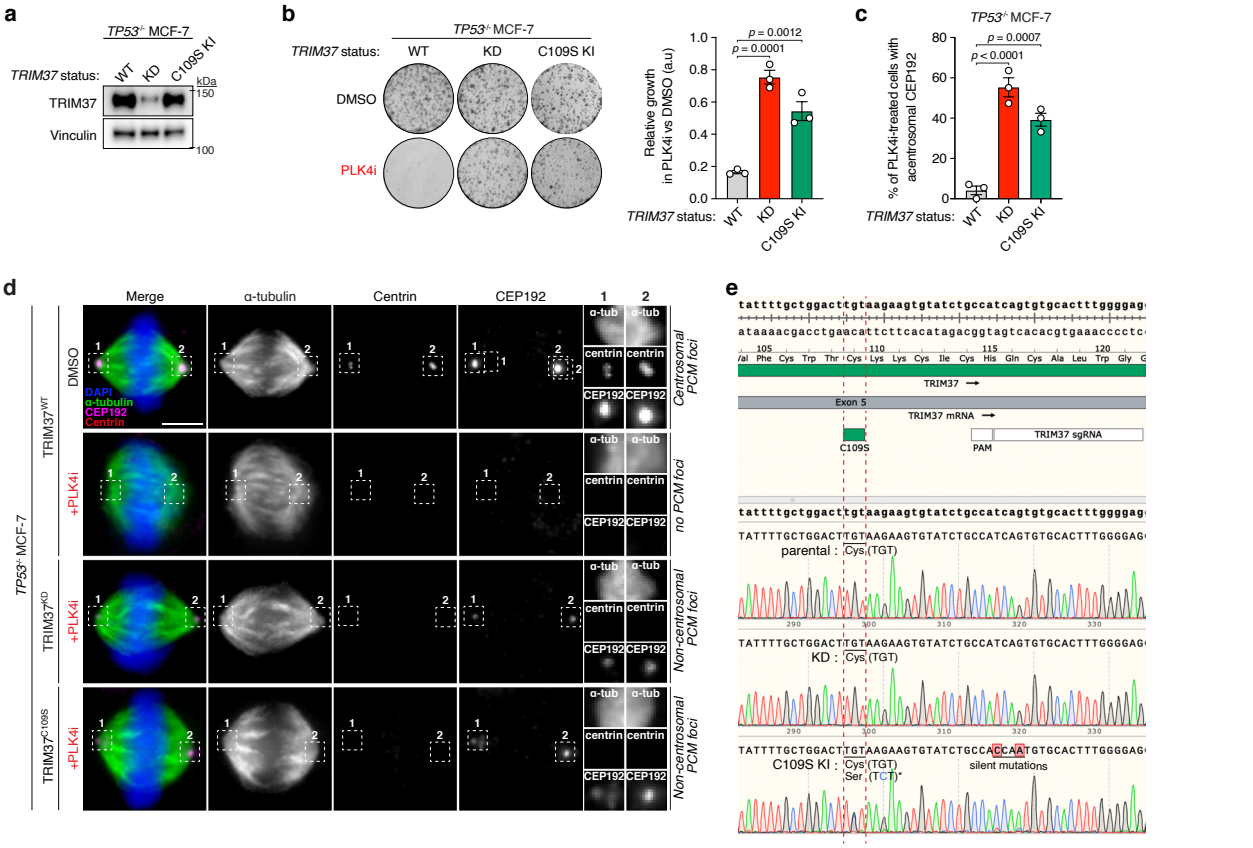

Extended Data Fig. 4 | Impairment of TRIM37 oligomerization attenuates synthetic lethality with PLK4 inhibition in 17q23-amplified cells. (**a**) Immunoblot showing TRIM37 protein levels in *TP53*$^{-/-}$ MCF-7 cells. *TRIM37* wild-type (WT), *TRIM37* knockdown (KD) via shRNA, and cells harboring the C109S mutation in approximately half of the TRIM37 alleles present (*TRIM37*^{C109S}) were used. Vinculin, loading control. Representative data; $n = 3$ biological replicates. (**b**) Left, Representative data of a 10-d clonogenic survival of indicated MCF-7 cell lines from (**a**) treated with DMSO (control) or PLK4 inhibitor (PLK4i) (250 nM). Right, Quantification of relative growth in the presence PLK4i relative to DMSO. *P* values, one-way ANOVA with post hoc Dunnett's multiple comparisons test to evaluate differences between each experimental condition (KD and C109S) and WT. Mean ± s.e.m. (**c**) Quantification of mitotic CEP192 foci in PLK4i-treated *TP53*$^{-/-}$ MCF-7 cells that lack centrosomes. $n = 3$, biological replicates, each comprising >30 cells. *P* values, one-way ANOVA with post hoc Dunnett's multiple comparisons test to evaluate differences between each experimental condition (KD and C109S) and WT. Mean ± s.e.m. (**d**) Representative images for (**c**). Scale bars, 5 µm. (**e**) Representative Sanger sequencing traces for the *TRIM37* locus in parental *TP53*$^{-/-}$ MCF-7 cells subjected to *TRIM37* knockdown (KD) via shRNA, and CRISPR–Cas9 edited *TRIM37*^{C109S} KI cells. The mutation (TGT > TCT) leading to the C109S residue substitution is denoted by an asterisk. Silent mutations introduced to prevent re-editing are highlighted.

https://doi.org/10.1038/s41594-025-01540-6

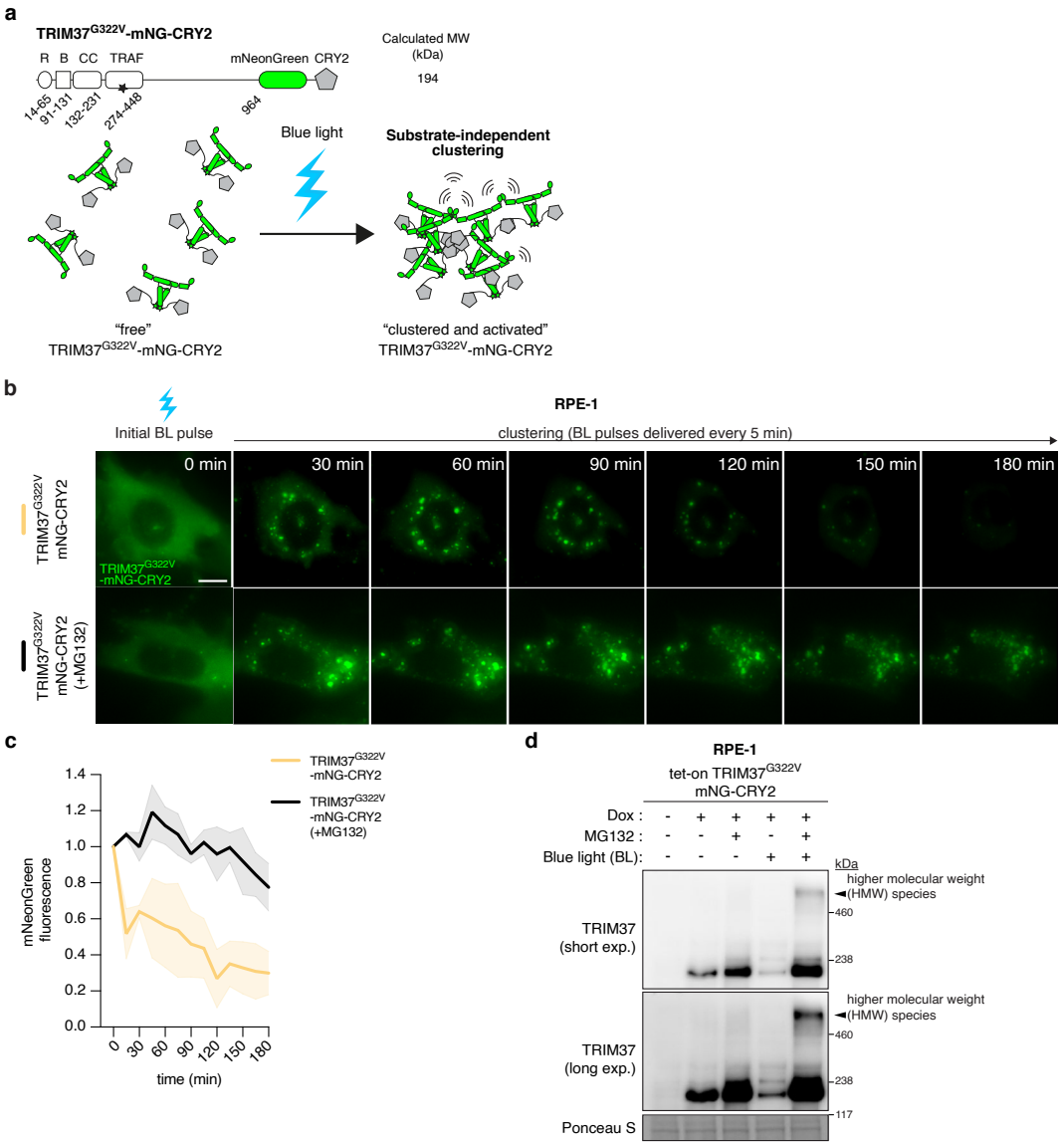

Extended Data Fig. 5 | Substrate-independent clustering is sufficient to activate TRIM37. Related to Fig. 7. (**a**) Top, schematic of the TRIM37^{G322V}-mNeonGreen-CRY2 optogenetic fusion construct. The star denotes the TRAF domain mutation (G322V). Bottom, illustration of the blue light (BL)- activated optogenetic system enabling TRIM37 clustering independent of binding to a centrosome substrate. (**b**) Representative time-lapse images of RPE-1 cells expressing the optogenetic construct detailed in (**a**) incubated in the presence or absence of MG132. Timestamps indicate minutes post blue light exposure. Scale bar = 10 µm. (**c**) Quantification of mNeonGreen fluorescence intensity from (**b**), with each condition comprising >30 cells. Mean ± s.d. (**d**) RPE-1 cells expressing optogenetic constructs detailed in (**a**) were incubated with or without doxycycline (Dox) and MG132 (10 µM) in the absence or presence blue light for 3 h before immunoblotting for the indicated proteins. Higher molecular weight (HMW) TRIM37 species were prominently formed only in MG132 and BL-stimulated conditions and are indicated with an arrow. Ponceau-stained blot indicates loading. Representative data; $n = 3$ biological replicates. exp, exposure.

nature portfolio

Corresponding author(s): Andrew J. Holland, Ph.D ., Zhong Yi Yeow, Ph.D

Last updated by author(s): Feb 19, 2025

Reporting Summary

Nature Portfolio wishes to improve the reproducibility of the work that we publish. This form provides structure for consistency and transparency in reporting. For further information on Nature Portfolio policies, see our Editorial Policies and the Editorial Policy Checklist.

Statistics

For all statistical analyses, confirm that the following items are present in the figure legend, table legend, main text, or Methods section.

n/a	Confirmed
☐	☒ The exact sample size (*n*) for each experimental group/condition, given as a discrete number and unit of measurement
☐	☒ A statement on whether measurements were taken from distinct samples or whether the same sample was measured repeatedly
☐	☒ The statistical test(s) used AND whether they are one- or two-sided *Only common tests should be described solely by name; describe more complex techniques in the Methods section.*
☒	☐ A description of all covariates tested
☐	☒ A description of any assumptions or corrections, such as tests of normality and adjustment for multiple comparisons
☐	☒ A full description of the statistical parameters including central tendency (e.g. means) or other basic estimates (e.g. regression coefficient) AND variation (e.g. standard deviation) or associated estimates of uncertainty (e.g. confidence intervals)
☐	☒ For null hypothesis testing, the test statistic (e.g. *F*, *t*, *r*) with confidence intervals, effect sizes, degrees of freedom and *P* value noted *Give P values as exact values whenever suitable.*
☒	☐ For Bayesian analysis, information on the choice of priors and Markov chain Monte Carlo settings
☒	☐ For hierarchical and complex designs, identification of the appropriate level for tests and full reporting of outcomes
☒	☐ Estimates of effect sizes (e.g. Cohen's *d*, Pearson's *r*), indicating how they were calculated

Our web collection on statistics for biologists contains articles on many of the points above.

Software and code

Policy information about availability of computer code

Data collection	Gel/membrane Imaging: GeneSys 1.8.10; Microscopy: SlideBook 2024
Data analysis	GraphPad Prism v9 was typically used for all presented statistical analyses; ImageJ version 2.14.0; UCSF ChimeraX version 1.6.1, AlphaFold-Multimer ColabFold (version 1.5.5), Jalview (version 2.11.4.1)

For manuscripts utilizing custom algorithms or software that are central to the research but not yet described in published literature, software must be made available to editors and reviewers. We strongly encourage code deposition in a community repository (e.g. GitHub). See the Nature Portfolio guidelines for submitting code & software for further information.

Data

Policy information about availability of data

All manuscripts must include a data availability statement. This statement should provide the following information, where applicable:

- Accession codes, unique identifiers, or web links for publicly available datasets
- A description of any restrictions on data availability
- For clinical datasets or third party data, please ensure that the statement adheres to our policy

The BioID MS proteomics data have been deposited in the ProteomeXchange Consortium via the PRIDE partner repository under accession number PXD061083. Source data are provided with the paper.

Research involving human participants, their data, or biological material

Policy information about studies with human participants or human data. See also policy information about sex, gender (identity/presentation), and sexual orientation and race, ethnicity and racism.

Reporting on sex and gender	N/A
Reporting on race, ethnicity, or other socially relevant groupings	N/A
Population characteristics	N/A
Recruitment	N/A
Ethics oversight	N/A

Note that full information on the approval of the study protocol must also be provided in the manuscript.

Field-specific reporting

Please select the one below that is the best fit for your research. If you are not sure, read the appropriate sections before making your selection.

☒ Life sciences ☐ Behavioural & social sciences ☐ Ecological, evolutionary & environmental sciences

For a reference copy of the document with all sections, see nature.com/documents/nr-reporting-summary-flat.pdf

Life sciences study design

All studies must disclose on these points even when the disclosure is negative.

Sample size	No statistical methods were used to predetermine the experimental sample size. All experiments with cell lines were performed with multiple biological replicates, based on prior experience with an optimized experimental setup. For microscopy-based assays, multiple fields of view were analyzed per biological replicate, ensuring a sufficient number of cells within each field for representative sampling.
Data exclusions	No data were excluded from the analyses.
Replication	Following extensive optimization, biological experiments were typically performed in 2-3 biological replicates (each performed identically on different days) with consistent results. In the majority of cases, each biological replicate (e.g. clonogenic assay,) involved 2-3 technical replicates. All attempts at replication were successful.
Randomization	Not applicable, as no group allocation was performed in any experiments. Experimental conditions were predefined and assigned based on the experimental design rather than random selection.
Blinding	Not applicable, as no group allocation was performed in any experiments, and data collection relied on objective quantification methods, eliminating the need for subjective analysis.

Reporting for specific materials, systems and methods

We require information from authors about some types of materials, experimental systems and methods used in many studies. Here, indicate whether each material, system or method listed is relevant to your study. If you are not sure if a list item applies to your research, read the appropriate section before selecting a response.

Materials & experimental systems

n/a	Involved in the study
☐	☒ Antibodies
☐	☒ Eukaryotic cell lines
☒	☐ Palaeontology and archaeology
☒	☐ Animals and other organisms
☒	☐ Clinical data
☒	☐ Dual use research of concern
☒	☐ Plants

Methods

n/a	Involved in the study
☒	☐ ChIP-seq
☒	☐ Flow cytometry
☒	☐ MRI-based neuroimaging

Antibodies

Antibodies used

Antibodies used in western blot studies:

Primary
Rb anti TRIM37: Bethyl, A301-174A, 1:1000
Rt anti HA: Roche, ROAHAHA, 1:1000
Ms anti b-actin :SantaCruz Biotechnology, sc-47778, 1:1000
Rb anti CEP192: home-made, 1:1000
Rb anti CNTROB: Atlas, HPA023319, 1:1000
Ms anti SAS6 :SantaCruz Biotechnology, sc-81431, 1:1000
Ms anti vinculin :SantaCruz Biotechnology, sc-73614, 1:1000
Ms anti GAPDH :SantaCruz Biotechnology, sc-47724, 1:1000
Rb anti TRIM37: Cell Signaling, #96167, 1:1000
Rb anti mCherry: Abcam, ab167453, 1:4000

Secondary
Horse anti-mouse HRP-conjugated: Cell Signaling, #7076; 1:1000
Goat anti-rabbit HRP-conjugated: Cell Signaling, #7074, 1:1000
Goat anti-rat HRP-conjugated: Cell Signaling, #7077; 1:1000
streptavidin HRP-conjugated: Cell Signaling, #3999; 1:1500

Antibodies used in Immunofluorescence studies:

Rt anti HA: Roche, ROAHAHA, 1:1000
Goat anti CEP192-Cy5: (raised against CEP192 a.a. 1-211), home made, 1:1000
Rb anti CNTROB: Atlas, HPA023319, 1:1000
Streptavidin Alexa Fluor™ 555 Conjugate : Invitrogen, S32355, 1:1000
Guinea pig anti β-tubulin: ABCD Antibodies, ABCD_AA344, 1:4000
Rb anti TRIM37: Cell Signaling, #96167, 1:1000
Ms anti Centrin: Millipore, 04-1624, 1:1000
Rt anti α-tubulin: Invitrogen, MA1-80017, 1:1000

Validation

All antibodies have been described and validated by their respective manufacturers for the purposes used in this study. Additionally, each experiment had appropriate controls to further validate the antibodies.

western blot studies: Rb-rabbit, Rt -rat, Ms -mouse

Rb anti TRIM37: Bethyl, A301-174A, 1:1000 https://www.fortislife.com/products/primary-antibodies/rabbit-anti-trim37-antibody/BETHYL-A301-174
Rt anti HA: Roche, ROAHAHA, 1:1000 https://www.sigmaaldrich.com/US/en/product/roche/roahaha?srsltid=AfmBOooqHD90EAY3_g9Mp1I19l1cqr_C-5qPOcaQL7iS6Ncmj5BIdG83
Ms anti b-actin: SantaCruz Biotechnology, sc-47778, 1:1000 https://www.scbt.com/p/beta-actin-antibody-c4?srsltid=AfmBOorrq5zHXfLAKn_j87ws9IXsXXU6EsFERdIb3hTksasz0cu5-FqX
Rb anti CEP192: home-made, 1:1000
Rb anti CNTROB: Atlas, HPA023319, 1:1000 https://www.atlasantibodies.com/products/primary-antibodies/triple-a-polyclonals/anti-cntrob-antibody-hpa023319-100ul/?language=en (Manucfacturer- IHC, this study- IF in Extended Data Fig. 1c , and Western blot in Fig. 4c)
Ms anti SAS6 :SantaCruz Biotechnology, sc-81431, 1:1000 https://www.scbt.com/p/sas-6-antibody-91-390-21?srsltid=AfmBOorFgPCwQwvaGqlSPnPl9QfjJlbCNS949JhQVCkWL8DIQ8F0pqmC
Ms anti vinculin :SantaCruz Biotechnology, sc-73614, 1:1000 https://www.scbt.com/p/vinculin-antibody-7f9?srsltid=AfmBOooEsYuYNoN8Mp6iNt6r33OxXutg_ZbGhEpWXl5kwlwdg-Qvc94A
Ms anti GAPDH :SantaCruz Biotechnology, sc-47724, 1:1000 https://www.scbt.com/p/gapdh-antibody-0411?srsltid=AfmBOopC2vMcMbRgl7Tr0rX27AQ5sLQftxVe1Di7xAftxD9TsOmy1_7L
Rb anti TRIM37: Cell Signaling, #96167, 1:1000 https://www.cellsignal.com/products/primary-antibodies/trim37-d7u2l-rabbit-mab/96167?srsltid=AfmBOopg-8Ga4J1QU9bNh6zlGs7lL9KOeHZhdwj8NbkW2KUN3NoUL78f
Rb anti mCherry: Abcam, ab167453, 1:4000 https://www.abcam.com/en-us/products/primary-antibodies/mcherry-antibody-ab167453?srsltid=AfmBOor8aSM0qo-DKQNYhv9Cuxh7mlDvXOzj3dyegKT7qiWJDLmdcqBq

Immunofluorescence studies: Rb-rabbit, Rt -rat, Ms -mouse

Rt anti HA: Roche, ROAHAHA, 1:1000 https://www.sigmaaldrich.com/US/en/product/roche/roahaha?srsltid=AfmBOooqHD90EAY3_g9Mp1I19l1cqr_C-5qPOcaQL7iS6Ncmj5BIdG83
Streptavidin Alexa Fluor™ 555 Conjugate : Invitrogen, S32355, 1:1000 https://www.thermofisher.com/order/catalog/product/S32355
Guinea pig anti β-tubulin: ABCD Antibodies, ABCD_AA344, 1:4000 https://abcd-antibodies.com/products/anti-beta-tubulin-antibody-abcd_aa344
Rb anti TRIM37: Cell Signaling, #96167, 1:1000 https://www.cellsignal.com/products/primary-antibodies/trim37-d7u2l-rabbit-mab/96167?srsltid=AfmBOopg-8Ga4J1QU9bNh6zlGs7lL9KOeHZhdwj8NbkW2KUN3NoUL78f
Ms anti Centrin: Millipore, 04-1624, 1:1000 https://www.sigmaaldrich.com/US/en/product/mm/041624?srsltid=AfmBOooqKiAOdVJ1yhZE2LCCZTS9jpomGeRyfWtp4kTevQfMRHQIyUR9D
Rt anti α-tubulin: Invitrogen, MA1-80017, 1:1000 https://www.thermofisher.com/antibody/product/alpha-Tubulin-Antibody-clone-YL1-2-Monoclonal/MA1-80017

The antibodies below have been described and validated in a previous study (Moyer & Holland, 2019 and Yeow et al, 2020).
Rb anti CEP192: (raised against CEP192 a.a. 1-211), home-made, 1:1000
Gt anti CEP192-Cy5 (raised against CEP192 a.a. 1-211), home-made, 1:1000

Eukaryotic cell lines

Policy information about cell lines and Sex and Gender in Research

Cell line source(s)	RPE-1 and MCF-7 parental cell lines (oringinally purchase from ATCC) were available in our lab and have been previously described (Yeow et al., 2020).
Authentication	RPE-1 (TRIM37-/-) cell line was validated in this study (Extended Data Figure 1). RPE-1 (TRIM37 C18R KI) cell line was validated in this study (Extended Data Figure 2). MCF-7 (TRIM37 C109S KI) cell line was validated in this study (Extended Data Figure 4) HEK293T cells were used as a packaging cell line for lentiviral production, respectively, and were not further authenticated.
Mycoplasma contamination	Yes - we maintain a very strict regime of mycoplasma testing, and no cell-line tested positive.
Commonly misidentified lines (See ICLAC register)	We have checked the ICLAC register and the cell lines used in our studies are not on the list of misidentified cell lines.

Plants

Seed stocks	*Report on the source of all seed stocks or other plant material used. If applicable, state the seed stock centre and catalogue number. If plant specimens were collected from the field, describe the collection location, date and sampling procedures.*
Novel plant genotypes	*Describe the methods by which all novel plant genotypes were produced. This includes those generated by transgenic approaches, gene editing, chemical/radiation-based mutagenesis and hybridization. For transgenic lines, describe the transformation method, the number of independent lines analyzed and the generation upon which experiments were performed. For gene-edited lines, describe the editor used, the endogenous sequence targeted for editing, the targeting guide RNA sequence (if applicable) and how the editor was applied.*
Authentication	*Describe any authentication procedures for each seed stock used or novel genotype generated. Describe any experiments used to assess the effect of a mutation and, where applicable, how potential secondary effects (e.g. second site T-DNA insertions, mosiacism, off-target gene editing) were examined.*